Strains in Fe/Cr/Fe trilayers and (Fe/Cr)5/Fe multilayers epitaxied on MgO and MgO/SrTiO3

G. Magnifouet, M. Vallet, E. Meslin, M. Walls, C. Bouillet, J. Arabski, V. Pierron-Bohnes

Strains in Fe/Cr/Fe trilayers and $(Fe/Cr)_5/Fe$ multilayers epitaxied on MgO and $MgO/SrTiO_3$

G. Magnifouet[a], M. Vallet[b,c,d], E. Meslin[b], M. Walls[e], C. Bouillet[a], J. Arabski[a], V. Pierron-Bohnes[a]

a. Université de Strasbourg, Institut de Physique et Chimie des Matériaux de Strasbourg (IPCMS), UMR 7504, BP 43, 67034, Strasbourg Cedex 2, France

b. Université Paris-Saclay, CEA, Service de recherche en Corrosion et Comportement des Matériaux, SRMP, 91191 Gif Sur Yvette, France

c. Now at: Université Paris-Saclay, CentraleSupélec, CNRS, Laboratoire SPMS, 91190, Gif-sur-Yvette, France

d. And at : Université Paris-Saclay, CentraleSupélec, ENS Paris-Saclay, CNRS, LMPS - Laboratoire de Mécanique Paris-Saclay, 91190, Gif-sur-Yvette, France

e. CNRS UMR 8502, Université Paris-Saclay, Laboratoire de Physique des Solides, F-91405 Orsay, France

Corresponding author: V. Pierron-Bohnes, vero@ipcms.unistra.fr

Université de Strasbourg, Institut de Physique et Chimie des Matériaux de Strasbourg (IPCMS), UMR 7504, BP 43, 67034, Strasbourg Cedex 2, France

Tel.: +33 630 582 521 or +33 388 107 073; Fax: +33 388 107 250

Abstract:

Fe/Cr/Fe trilayers and multilayers are prepared as model systems designed to furnish simple data comparable with calculation results for diffusion properties in nuclear materials. Their structure (epitaxy, residual strains and dislocations) is characterized in detail. The film structure (strain and stress) is shown to be different on $MgO_{20nm}/SrTiO_3$ and MgO substrates due to the residual strain in the MgO buffer layer on $SrTiO_3$. Superlattices with high crystalline quality are prepared, with Fe and Cr in coherent epitaxy. In-plane residual strain in Fe is +0.45(13)% on MgO substrates and decreases from 1.70(9)% to 0.47(2)% when increasing the thickness of the trilayers on $MgO/SrTiO_3$ substrates. These strains enhance the contrast between Fe and Cr, opening the way to future kinetics studies using x-ray diffraction in this system, which is far more efficient (non-destructive and rapid) than high resolution transmission electron microscopy with electron energy loss spectroscopy or atom probe tomography.

Keywords: Superlattices; Iron/Chromium; Residual strain; Epitaxy dislocations; X-ray diffraction; Scanning transmission electron microscopy; Electron energy loss spectroscopy; Atom probe tomography

68.65.Cd (Superlattices), 68.37.−d (Microscopy of surfaces, interfaces, and thin films), 61.72.Ff (Direct observation of dislocations and other defects (etch pits, decoration, electron microscopy), x-ray topography, etc.)), 61.72.Hh (Indirect evidence of dislocations and other

defects (resistivity, slip, creep, strains, internal friction, EPR, NMR, etc.)), 79.20.Uv (Electron energy loss spectroscopy), 61.05.C− (X-ray diffraction and scattering)

Competing interest statement: the authors have no competing interests to declare.

1) Introduction

Cr-rich ferritic martensitic steels are potentially useful as structural or cladding materials for the next generation of nuclear power plants (NPP) (generation IV and fusion reactors) [1-3]. The addition of Cr prevents corrosion and the FeCr ferritic form is resistant to swelling and atomic segregation under high-energy neutron irradiation. Many teams have studied the electronic structure of these alloys in order to understand the origin of this unusual behaviour [4-7] that has often been attributed to chemical and magnetic short-range order effects [8-12]. To predict the behaviour under radiation of this alloy, it is necessary to obtain diffusion properties of this material at the operating temperature of NPP, close to $T_m/3$, where T_m is the melting temperature. At such low temperatures, the diffusion length of elements in a reasonable timescale is too low to use the classical micron-scale diffusion couples. As a consequence, the aim is to use nanoscale multi-layers to reach nanometer scale interdiffusion coefficients. In this paper, we describe the preparation of Fe/Cr/Fe trilayers and multilayers with flat interfaces and limited defects and strains, designed as model systems that can furnish simple data comparable with calculation results of atomic interdiffusion.

Fe/Cr superlattices generated scientific interest at the end of the last century because of the magnetoresistance behaviour discovered by Peter Grünberg et al. [13] and Albert Fert et al. [14]. Since this discovery, many researchers have grown Fe/Cr multilayers. To our knowledge, the stress effects have only been studied in Co/Cu systems. Up to now, no Fe/Cr multilayers grown on MgO(100) substrates using molecular beam epitaxy (MBE) have been reported; only sputtering has been used [15-17]. Moreover, no study has been published describing epitaxial Fe/Cr(100) on MgO buffer layers on $SrTiO_3$(100) substrates, despite this

system having a smaller lattice mismatch with Cr and Fe than a bulk MgO(100) substrate [18-21]. $SrTiO_3$ (STO) is also an easier substrate to deal with for the preparation of transmission electron microscopy (TEM) cross-sections and atom probe tomography (APT) tips.

This paper reports the preparation of Fe/Cr/Fe trilayers and multilayers on MgO and STO substrates and the detailed study of their structural properties. We show that high-quality superlattices can be prepared and that, because of the strains, the contrast between Fe and Cr is enhanced, which opens the way to kinetics studies using x-ray diffraction (XRD) in this system.

2) Experimental techniques

Fe/Cr/Fe tri-layers and Fe/Cr multilayers were deposited by molecular beam epitaxy in a high-vacuum chamber equipped with an ionic pump and cryogenic double walls (liquid N_2) with a base pressure of about 10^{-8} Pa. The pressure during MgO deposition reached 6. 10^{-7} Pa while during Fe and Cr deposition it was 6 and 4. 10^{-8} Pa respectively.

The system is equipped with two electron guns dedicated to MgO, Cr and Au on the one hand and Fe on the other. High-purity evaporation sources (3N5 MgO, 6N Fe and Cr, and 5N Au) were used for deposition; slow deposition speed (0.02 nm/s) was used for all layers. Reflection High-Energy Electron Diffraction (RHEED) was used at some steps of the growth to get information on the surface quality. The thicknesses of the Fe and Cr layers were monitored using a quartz balance localised in the flux, whereas MgO and Au thicknesses were monitored via deposition time (to spare the quartz balance as the atomic weight of Au is high). The

surface roughness was also observed using atomic force microscopy (AFM) at some growth steps on test samples.

The surface roughness at different stages of the growth was studied using a Bruker Dimension Icon atomic force microscope in tapping mode.

Both TEM and APT samples were prepared using focused ion beam (FIB) with an FEI Helios dual beam Nanolab 650 equipped with a Ga liquid metal ion source. A layer of platinum was deposited on the surface of samples before any ion observation to preserve the surface layers. TEM studies were made on cross-sectional samples prepared using FIB. For electron energy loss spectroscopy (EELS), a very thin sample is necessary to avoid multiple scattering; for that reason, some additional Ar-ion milling using a PIPS II (precision ion polishing system from Gatan) was used (with a low angle and a low ion-energy).

APT analyses were performed using a CAMECA LEAP 4000XHR at a set-point temperature of 50 K in laser-pulsing mode at a wavelength of 382 nm, 200 kHz pulse repetition rate, and 40 pJ pulse energy. For 3D atom reconstruction, visualization and data treatments, the IVAS software by CAMECA was employed. Reconstructions of the volumes were performed using spatial distribution maps on low index crystallographic poles [22].

For conventional TEM experiments, we used a JEOL 2100F microscope, operated at 200 kV, equipped with a Schottky electron gun (point to point resolution: 0.2 nm). Scanning transmission electron microscopy (STEM) imaging in bright and dark field mode was carried out on an FEI TITAN3 transmission electron microscope operating at 300 kV. It contains a condenser lens equipped with an advanced set of magnetic lenses dedicated to the reduction of spherical aberration (*C*s), enabling a spatial resolution in STEM of 70 pm.

High resolution STEM in high-angle annular dark-field (HAADF) mode [23,24] and EELS analyses [25] were performed in a Nion Ultrastem 200 cold FEG microscope operating at 100 kV. The *C*s-corrected probe attains 75 pm in HAADF imaging and around 0.5 nm in EELS elemental maps in our conditions. The electron spectrometer has a Merlin MEDIPX3 direct electron detector and the operating conditions gave an energy resolution of around 1 eV. EELS spectrum-images were recorded using a beam current of around 50 pA and a pixel dwell time of 10 ms. We used the L_{23} edges for Cr (575 eV) and Fe (710 eV) to quantify the concentration of each element. The quantification was performed using Hyperspy [26], based on the use of internal standards generated via independent components analysis, rather than using calculated inelastic scattering cross sections [27]. This enables a more confident measurement of the absolute concentrations. Oxygen (532 eV) is detected in very small quantities on the multilayers, consistent with some surface oxidation of the FIB lamellae.

Texture, mosaicity, epitaxy quality, and residual stress were determined using a four-axis RIGAKU x-ray diffractometer operated at 45 kV and 200 mA equipped with a rotating Cu anode and a Ge(220) crystal monochromator to select Cu-Kα_1. The beam divergence was 0.03°. $\theta/2\theta$ scans at wide angles were performed to determine the preferential orientation of the film. Rocking curves (ω-scans) give information on the mosaicity (a FWHM below 1° is satisfactory for metals). The epitaxial quality of the layers was determined by measuring pole figures. The average in-plane and out-of-plane residual strains of Fe and Cr were measured using the $\sin^2(\psi)$ method on (200), (110), (220), (130), (310), (222), and (211) reflections. The in-plane stress and the swelling were deduced.

3) Preparation

(100)-oriented $SrTiO_3$ and MgO were chosen as substrates because a coherent epitaxy is favoured by the small lattice mismatch between these materials and Cr/Fe, when a 45° rotation is performed. The iron lattice parameter (a_{Fe}^{bulk} = 0.28684 nm = 0.4057/$\sqrt{2}$ nm) with a 45° rotation has a -3.7% mismatch on MgO [28] (a_{MgO} = 0.42112 nm) and a +3.9% mismatch on STO (a_{STO} = 0.3905 nm). The chromium lattice parameter (a_{Cr}^{bulk} = 0.2884 nm = 0.4079/$\sqrt{2}$ nm) is very close (+0.54% mismatch with Fe), and the epitaxy conditions are equivalent. The substrates were provided by Crystal-GMBH (Berlin) for both MgO and STO. The main impurities reported by the provider are in MgO: Ca (200 ppm), Fe (48 ppm), Al_2O_3 (45 ppm), and Si (36 ppm); in STO: only Si (60 ppm) and Ba (16 ppm) have a concentration above 10 ppm. MgO(100) and STO(100) substrates were mounted symmetrically on the same rotating metallic plate and deposition was made simultaneously on both. Before the growth, the substrates were heated to 723 K for 15 hours (to let the volatile impurities diffuse from the interior of the substrate towards the surface) and to 873 K for 20 minutes (to evaporate these impurities and clean the surface). A 20 nm-thick MgO buffer layer was deposited at 873 K on both types of substrate. As shown by XRD on samples deposited with and without the MgO buffer layer in Appendix B, on STO the buffer MgO layer is necessary to obtain the epitaxy. On the MgO substrate, it buries any remaining surface impurities [29] and improves the surface quality, as verified by RHEED patterns (not shown). Fig. 1 presents some AFM images on degassed substrates and on the MgO buffer layer. The surface is indeed improved by the buffer layer deposition, which smooths the steps on STO substrates and buries the 5 nm-high islands present after

annealing on MgO substrates (islands located on scratches or steps). This method has been successfully used for some time at the IPCMS in Strasbourg and the Institut Lamour in Nancy to prepare atomically flat tunnel barriers on MgO [30-32].

A series of trilayers was studied. The first layer was iron, deposited at room temperature (RT) to avoid oxidation reaction at the interface with the buffer layer and subsequently annealed for 2 h at 773 K to improve flatness and crystallinity. After cooling down, the Fe/Cr bilayer and the covering gold layer were deposited at RT. Fig. A1 in Appendix A shows the RHEED images of the first Fe layer deposition before and after annealing. The smoothness is indeed improved by the heat treatment. The chromium layer and the second layer of iron are slightly rougher but the surface quality is still good. The RHEED patterns (not shown) acquired after deposition confirmed that the multilayers were flat and highly epitaxial, as was the subsequent RT-deposited Au layer in most cases.

In this paper, A/B denotes an A layer deposited on a B layer. T*X*F*Y* indicates the trilayer Au_*y*/Fe_*Y*/Cr_*Y*/Fe_*Y*/MgO_*z*/*X*O, with *Y* = 2, 5, 10, 15, 20, 25, 30 nm (*X*O = MgO or STO; in the names *X* = M for MgO and S for STO). For comparison, the buffer layers B*X*F*Y* = Au_*y*/Fe_*Y* /MgO_*z*/*X*O with *Y* = 5, 10, 20 nm were prepared. For APT, EELS-STEM and future interdiffusion studies, multilayers F*Y*10 = Au_*y*/(Fe_*Y*/Cr_*Y*)$_5$/Fe_*Y*/MgO_*z*/*X*O with *Y* = 10 nm were also prepared on both substrates. In all multilayers, *z* is around 20 nm and *y* around 5 nm.

4) Architecture and chemistry of the layers

As an example, Fig. 2a shows a bright field STEM imaging of the nanometer scale arrangement of the Fe and Cr layers in MSF10. The thickness of both the Fe and Cr layers is about 9.5 nm with a fluctuation of 0.3 nm. The layers appear very flat. The multilayers present some diffraction contrast inside the layers. We attributed this contrast to dislocations that cross all the layers. The misfit dislocations generated at the MgO/STO interface and at the Fe/MgO interface are studied in §7.

APT was performed to determine the chemical composition within the Fe/Cr multilayers. Figs. 2b and 2c show APT results obtained on MSF10. The layers are homogeneous in composition, suggesting that the defects observed by TEM are not due to chemical composition differences. The atomic composition of each layer has been measured in the middle of layers (averaged over 2.5 nm) to prevent any APT artefact at interfaces due to the difference of evaporation field between Fe and Cr which may produce some local compression or tension of the ion trajectories [33]. This artefact also induces a wrong apparent thickness difference. Results show a purity level higher than 99.7% for all the Fe and Cr layers. The oxygen distribution was also analysed due to its high reactivity with Cr. Oxygen levels remain extremely low throughout the sample. The oxygen is mainly localized at interfaces with a local maximum composition at 2%. The location of every detected oxygen atom is shown on the top of Fig. 2c. The Fe layers are almost free of O and the Cr/Fe interfaces (note the growth direction from the right towards the left on the image) are the most polluted by O, as probably the oxygen atoms of the vacuum chamber are trapped by the Cr evaporation source during Fe deposition and by the Cr layer during the waiting time to change electron gun and/or to perform RHEED experiment (≈250 s each) [34]. Concerning the C and N distributions, levels remain extremely low and never exceed 0.1% for the whole

volume. This low contamination may come from the residual gases of the UHV chamber during the layers' deposition. Fig. 2d shows the chemical maps obtained by EELS which confirm (with lower precision) the APT findings (> 98% purity for the layers).

Reflectometry measurements give information on the thickness and roughness of the layers. The Fe and Cr layers have similar electronic densities and cannot be separated using reflectometry with a Cu anode, thus only the total thicknesses and the roughness above the last 3d-metal layer only are determined. The total Fe/Cr/Fe trilayer thicknesses e_R are 5% smaller than the nominal value (in agreement with STEM observations). In TSF*Y*, we found a root mean square (RMS) roughness of 0.2-0.3 nm at the STO surface and of 0.05-0.25 nm at the MgO buffer surface. In TMF*Y*, the RMS roughness at the MgO buffer surface is 0.2-0.95 nm. At the Au/Fe interface, the RMS roughness is 0.2-0.5 nm in TMF*Y*, and 0.1-0.2 nm in TSF*Y*. Some examples of curves and fits are shown in Fig. 3.

5) **Crystalline quality**

Fig. 4 shows the global high-angle $\theta/2\theta$ scans of B*X*F*Y* buffer layers, T*X*F*Y* tri-layers for the different *Y*, and M*X*F10 multilayers. Besides the (*h*00) reflections of the substrates, the MgO buffer layer in BSF*Y*, TSF*Y* and MSF10, and the Au coverage, the (200) reflections of Fe and Cr layers are intense, indicating a good (100) texture of Fe and Cr films along the [100] direction of the substrate. Due to the used wavelength, the (400) reflections of Fe and Cr are not accessible. There is a single (200) peak in this range for the buffer layers and the thinnest trilayers (for thin layers, the width of the peaks is large, preventing any fine structure from appearing). For *Y* > 10 nm, the intensity is separated into two peaks presenting a modulation

due to interferences. In the multilayers, satellites due to the alternating Cr and Fe layers are present. Note the Laue fringes around the (200) Au Bragg peak at 44.4° in $\theta/2\theta$ scans of T*X*F*Y* samples with a period corresponding to the Au thickness (5 nm or 9 nm depending on the sample). Their presence indicates a very good flatness of the layer. They are negligible around the other peaks due to the small density contrast at the other interfaces.

The rocking curve full widths (Fig. A2a) are smaller than 0.5° for $Y \geq 10$ nm, indicating a very good crystalline quality (mosaicity smaller than 0.5°) and a large in-plane coherence length (larger than $L_{//}=2\pi/\Delta Q_{//} \approx 20$ nm with $Q_{//}=\Delta\omega\, Q$ and $Q= 4\pi \sin(\theta)/\lambda$). The thicker the layers, the narrower the rocking curve width; hence the mosaicity and/or lateral coherence length improve during the growth.

To determine the epitaxial relationship, pole figures were measured for the {110} plane families of Fe and Cr (Fig. A3). Because the substrates have a four-fold symmetry, quarter pole figures were sufficient. For all layers, we observe a single intense and narrow (110) spot around the angles $\phi = 45°$ (from the (020) peak of the substrate) and $\chi = 45°$ corresponding to the epitaxy relationship [35] *M*(100)[011] // *X*O(100)[010] for *M*=Fe or Cr and *X*O=MgO or STO. The same epitaxial relationship was obtained by Fullerton *et al*. [17,36,37] for Cr/Fe multilayers grown on MgO(100) by magnetron sputtering, but with a poorer crystalline quality. All the pole figures were measured in the same conditions, so we can compare their intensities. In Fig. A3c, the intensity of the (110) peak increases more rapidly than the thickness, indicating that the global epitaxy improves with *Y*.

High resolution images were acquired from different cross-sectional samples with the electron beam direction along $[001]_{STO}$ and $[001]_{MgO}$. The (100) planes of Fe, MgO and STO are observed, indicating a good epitaxy of Fe and MgO on STO (Fig. 5a, Figs. 9 in §7). Electron

diffraction patterns (Fig. 5b) show the expected spots for Fe, MgO and STO in both $[010]_{STO}$= $[010]_{MgO}$= $[011]_{Fe}$ (in-plane) and $[100]_{STO}$= $[100]_{MgO}$= $[100]_{Fe}$ (out-of-plane) directions, confirming the good epitaxy of the MgO and Fe layers on the substrate as well as the epitaxy relationships.

6) Strains

6.1 Out-of-plane strains

In a first approximation, the coherence length of the (200) periodicity can be estimated from the widths of Gaussian fit to the peaks. In the buffer layers, the widths of the peaks correspond to a coherence length similar to the nominal thickness. In the thickest trilayers (Figs. A2b) the two main peaks are sufficiently separated to provide individual coherences. The coherence length corresponds to the total thickness in the two thinnest trilayers, whereas in the TMF15 and TMF30 trilayers, the three layers diffract incoherently ($L_\perp$=e_R). In the other trilayers, the coherence length is larger than Y, meaning that the interferences between the different diffracted beams have to be considered to simulate the curves. The trilayers have thus to be considered as multilayers.

Fig. 6 shows zooms on the (200) Fe,Cr reflections. Due to the interference effects, the scans are not a superposition of the individual peaks of Fe and Cr layers. They can be simulated with 5 independent parameters: N_1, N_2, N_3: the numbers of atomic layers in individual layers (N_3 Fe planes on N_2 Cr planes on N_1 Fe planes), $a_{Fe\perp}$ and $a_{Cr\perp}$, the lattice parameters in the growth direction in the Fe and Cr layers. The set of parameters has been adjusted to make a

least square fit to the experimental curves (see Annex C). In the simulations, we assume absolutely abrupt and planar interfaces with an interplanar distance at the interface: (a_{Fe} + a_{Cr})/2. The numbers of atoms per unit surface were assumed equal for Fe and Cr (indeed, we show in §6.2 that the in-plane lattice parameters are equal). The interference scattering simulations use the anomalous scattering coefficients (see appendix C).

A first fit with the constraint N_3=N_1 was performed and gave quite satisfactory results. The Fe thickness (Fig. A2-c,d) is found to be less than a third of the thickness deduced from reflectometry (this effect is the largest in TMF25 and TSF25), showing the presence of an initial Fe layer with many defects, and so not perfect enough to be in coherence with the rest of the trilayer (in agreement with the STEM observations of §6). In a second step, the constraint was released. The lack of coherence in the first few Fe planes near the Fe/MgO interface diminishes N_1 ($N_1 < N_3$). The χ^2 of the fit decreased by about 20% for T*X*F*Y* with $10 \leq Y \leq 25$. The thin red lines in Fig. 6 show the result of this fit for those trilayers and the result of the simpler fit (N_3=N_1) for T*X*F5 and T*X*F30 trilayers.

The Cr thickness (Fig. A2c,d) is close to the value deduced from reflectometry (e_R/3), except for T*X*F25, indicating that in these trilayers the crystallographic coherence length is smaller than the layer thickness. The thickness of the thicker Fe layer is slightly smaller than e_R/3 and that of the thinner is 20% smaller. The lattice parameters deduced from the fits (Fig. A2e,f) are not sensitive to the constraint N_3=N_1. The Cr lattice parameter is very close to the bulk value. The Fe lattice parameter is smaller, in agreement with the out-of-plane strain in compression expected for an in-plane strain in tension. The strain in the Fe layers is more or less constant on the MgO substrate and larger for the thinnest layers on the STO substrate.

The $\theta/2\theta$ scans on the MMF10 and MSF10 multilayers (Fig. 6c,d) present many satellites (the orders -4, 4 and 6 are clearly visible in MSF10 where the signal/noise ratio was the best). This confirms that the multilayers are superlattices. There is a small shift of the peaks in MSF10 compared to MMF10, indicating a difference in average out-of-plane strain in the Fe/Cr multilayer of 0.19(1)%. The distances between the satellites are the same because the periods are equal, in agreement with the STEM observations. The simulations have been optimized using the same method as in the trilayers: N_1 Fe layers covered by 5 (N_2Cr+N_3Fe) bilayers. The optimum is obtained for N_1=46, N_2=70, N_3=64 in both samples, a_{Fe} = 0.28452 nm, a_{Cr} = 0.28857 nm in MMF10 and a_{Fe} = 0.28397 nm, a_{Cr} = 0.28847 nm in MSF10. These lattice parameters are close to those obtained in TMF10 and TSF10 respectively (Fig. A2e,f). The fit is satisfactory considering the simple description of the multilayers (integer numbers of atomic layers in the layers, abrupt interfaces). The bilayer thickness is 19.2 nm (9.1 nm of Fe and 10.1 nm of Cr) in both samples. Note that the difference in strain is responsible for the contrast between Fe and Cr layers in the superlattices. As a matter of fact, Fig. A4 shows that with diffraction contrast alone, the satellites would have very small intensities, preventing any precise study.

6.2 In-plane strains

For all samples, intensity maps in reciprocal space were measured around several non-specular peaks (***Q*** makes an angle α with $\boldsymbol{u_1}$ the unit vector along the normal to the sample) to estimate the in-plane strains (Fig. A5a,d). Non-specular peaks can be measured with $\theta/2\theta$ scans, varying either $\omega = \alpha + \theta/2$ (rotation of the normal of the sample inside the diffraction plane; limited by the condition $\omega > 0$, i.e. reflection mode; the explored plane in reciprocal

space contains $\boldsymbol{Q}$ and $\boldsymbol{u_1}$) or ψ (rotation of the sample normal out of the diffraction plane; no limitation but poorer resolution; the explored plane in reciprocal space contains $\boldsymbol{Q}\times\boldsymbol{u_1}$ and $\boldsymbol{Q}$). The interference satellites are clearly separated from the main peak only in the first method. For multilayers, satellites are observed for (200), (211) and (220) peaks (Fig. A5a,b). The satellite peaks are not resolved for (310), (222) and (130) peaks measured when varying ψ (Fig. A5c,d). For trilayers, the small oscillations observed in $\theta/2\theta$ (Fig. 6) are not resolved on non-specular peaks. A single Fe/Cr/Fe peak is observed for all trilayers for (310), (222) and (130) and for thin trilayers (TMF2, TMF5, and TSF2) for all (*hkl)*. Two peaks (one for Cr and one for Fe) are resolved in the thick trilayers for (200), (211) and (220). The 2θ values of the peaks are deduced from least square fits with Gaussians in *2D.* The same fit to one or two gaussians is applied here also to the (200) peak. This simplification is necessary to use the $\sin^2(\psi)$ method to determine the in-plane strains.

Fig. 7 shows $\sin^2(\psi)$ plots in B*X*F*Y*, T*X*F*Y* and M*X*F10 (*X* = M and S). The different plots of Fig. 7b and Fig. 7d are split in Fig. A6 and Fig. A7 respectively. The dashed-dotted horizontal lines show the Fe and Cr lattice parameters in the bulk. When the Cr and Fe peaks can be separated, two slopes are observed. As the low-α peak is observed in the Fe buffer layers and as $a_{Cr\_bulk} > a_{Fe\_bulk}$, we attribute the highest *a* values to the Cr layer and the lowest to the Fe layer. The points are fitted with a straight line to deduce the in-plane ($\sin^2(\psi)=1$) and out-of-plane ($\sin^2(\psi)=0$) lattice parameters. It is noticeable that both in-plane lattice parameters are equal (within the error bar) for the lines attributed to Fe and Cr, meaning that Fe and Cr layers grow coherently. Fe is stressed in tension in-plane whereas Cr is almost relaxed in-plane in thick samples on both substrates.

In the B*X*F*Y* buffer layers, we observe a positive slope with an in-plane tension strain as expected on an MgO buffer layer with an in-plane lattice parameter 0.5-1% larger than in bulk. A compressive out-of-plane strain is induced through Poisson's effect. Assuming no swelling (the swelling expected for a 0.3% O concentration in Fe layers is 0.02% with the calculated size factor [38] of O in *bcc* Fe: *SF* = 0.176 [39]; we will neglect it as it is smaller than the experimental error bars), the deduced Poisson's coefficients ν are 0.378(96), 0.350(81), 0.397(31) for BMF*Y* and 0.309(23), 0.388(28) and 0.401(25) for BSF*Y* (*Y* = 5, 10, 20 nm respectively). Except in BSF5, these values are in good agreement with the values calculated by D. Sander [40] from elastic constants: ν = 0.37. A Poisson's coefficient ν equal to 0.37 means $\varepsilon_{//} / \varepsilon_{\perp} = -(1-\nu)/2\nu = -0.85$ and that the swelling can be read on the curves around $\sin^2(\psi) = 0.55$, which is indeed the value where all lines cross the bulk Fe line, except in BSF5. We can thus deduce a small positive swelling in BSF5.

The in-plane strains $\varepsilon_{//}$ of Fe in all layers are shown in Fig. 8 and given in Table 1. It is constant on MgO substrates and decreases with *Y* on STO.

The non-specular peaks of the MgO buffer layers are very close to those of Au and the in-plane lattice parameter could not be measured directly. We deduced it from the out-of-plane lattice parameter with a Poisson's coefficient of ν(MgO) = 0.178(9) [41] ($\varepsilon_{//} / \varepsilon_{\perp} = -(1-\nu)/2\nu = -2.31(14)$). The MgO layer is found to be in compression in plane with a strain around -0.4%. The in-plane strains in MgO buffer layers are plotted in Fig. 8 and given in Table 1 for comparison with those in the Fe layers.

For trilayers, assuming a Poisson's ratio of 0.37, the Fe lines in Fig. 7, A6 and A7 are compatible with a zero swelling (except in TSF2 and TSF5). The Cr lines have very small slopes, so the Cr layers are almost relaxed. In the multilayers, the average peak and first

superlattice satellites have been reported. The lines converge towards a unique in-plane lattice parameter. The strains of all layers on the MgO substrate are around the same value with an average of $<\varepsilon_{//}(Fe)_{MgO}> = 0.45(13)\%$ in Fe (not considering TMF2). On the STO substrate the strain varies in Fe, increasing at small values of *Y*. Note that the points are on a single $<\varepsilon_{//}(Fe)_{MgO}>+A/Y$ curve (Fig. 8) for the buffer layers, the trilayers and the multilayers on STO, which shows that the important parameter to describe this supplementary strain, compared to the layers prepared on MgO substrates, is the thickness of individual layers and not the total thickness. We deduce that the first Fe layer is different on STO.

7) Dislocations

At the MgO/STO interface, if the strain was totally relaxed, the misfit m=7.8% would give rise to one missing plane in MgO every 13 STO atomic planes ($1/m$=12.75), i. e. dislocations with separation d = 2.685 nm. At the Fe/MgO interface, the misfit m = -3.7% corresponds to one half plane added in Fe every 27 MgO atomic layers ($1/m$=27.1), or d = 5.52 nm. These epitaxy dislocations give rise to extended defects, threading dislocations, corresponding to the ends of these half-planes that are not infinite. These defects are responsible for the contrast observed in Fig. 2a. In the samples deposited on STO, some dislocations created at the MgO/STO interface may be annihilated at the Fe/MgO interface. When the samples are annealed, the presence of extended defects will have a strong influence on the diffusion and so it is important to characterize the epitaxy dislocations in detail. Moreover, XRD detected some residual strain in the MgO buffers and in Fe layers. It is interesting to compare them to the strain deduced from the dislocation numbers at the two interfaces.

We therefore acquired high resolution STEM-HAADF images from MSF10. Fig. 9a shows the interface between the STO substrate and the MgO buffer layer. To evidence the dislocations and get a good statistic, seven images have been Fourier filtered (using Fast Fourier transform – FFT, a mask, and inverse FFT – iFFT – in DigitalMicrograph® from Gatan). Using a mask selecting the (020) peaks of STO and MgO (Fig. 9c), we reveal the epitaxy dislocations (Fig. 9b). They are marked by a 'T' (additional half plane below) or a '⊥' (additional half plane above). When dislocations are in close pairs with opposite Burger's vectors, they are probably artefacts. Moreover, they depend on the applied mask diameter. They are marked in yellow. The true epitaxial dislocations are marked in red. They are regularly distributed at the MgO/STO interface. The position of the interface is deduced from the disappearance of the STO periodicity in Fig. 9a. Most dislocations are located at the interface and only a few artefacts are present. The true dislocations were counted and their numbers were confirmed by counting the planes between the red arrows in STO and MgO. The average distance between dislocations was measured in the 7 different images. The distribution is shown as narrow blue bars in Fig. 10a. The distances between the dislocations and the interface were measured and the corresponding distribution is shown as narrow blue bars in Fig. 10c. Many dislocations have migrated into the STO substrate.

The same analysis was performed at the Fe/MgO interface on 5 images. The location of the interface is deduced from the strong dark/bright contrast present in the HAADF image (Fig. 9d). The misfit dislocations were imaged with a mask on the $(011)_{Fe} \approx (020)_{MgO}$ peaks (green in Fig. 9g). The dislocations are not regularly distributed (Fig. 9e) and there are many spurious dislocations. Many epitaxy dislocations are located inside the Fe layer. The interface is thus not the preferred location for dislocations. This agrees with the observation that the

first Fe layer is only partly in coherence with the rest of the trilayers or multilayers, as deduced from the x-ray diffraction simulations of $\theta/2\theta$ scans. Moreover, the distance between two dislocations is larger and fluctuates a lot (thick beige bars in Fig. 10a). The error bar on the deduced residual strain (Fig. 10b) is so large that even its sign cannot be deduced from these images. The average distance of the dislocations from the Fe/MgO interface (thick beige bars in Fig. 10c) is around 1 nm. Note that the image displays only 5 nm of Fe. As the dislocations are dispersed in the Fe layer, this field of view may not be sufficient to observe all the dislocations, which would explain the discrepancy between TEM and XRD results in terms of in-plane strains. We did not detect any dislocation at the Cr/Fe interface, which is unsurprising because the in-plane lattice parameters of Fe and Cr are equal as deduced from asymmetrical x-ray diffraction.

In *bcc* metals, two types of dislocations are stable, with Burger's vector of ½<111>-type and <001>-type respectively [42]. Both Burger's vectors have the same ½[011] projection along the interface line in Fig. 9d. To distinguish between these two possibilities, we imaged the dislocations with the Burger's vector perpendicular to the interface with a mask on the $(200)_{Fe,MgO}$ peaks (magenta in Fig. 9g) to have an insight into the perpendicular component of the dislocation Burger's vectors. We observe in Fig. 9f that the misfit dislocations detected in Fig. 9e do not have such a component. We deduce that the misfit dislocations have a *b*=<001>-type Burger's vector within the Fe/MgO interface.

8) Discussion

The multilayers have an excellent crystalline quality on both substrates. In this paragraph, we will discuss the strain results from both x-ray diffraction and high-resolution STEM (HRSTEM).

X-ray diffraction showed:

- identical in-plane lattice parameter for Fe and Cr,
- residual in-plane strain of +0.45(13)% in the Fe layers and Fe/Cr/Fe trilayers epitaxied on MgO substrate,
- residual in-plane strain of -0.37(11)% in the MgO buffer layer epitaxied on STO substrate,
- *Y*-dependence of the in-plane strain in the Fe and Cr trilayers deposited on MgO/STO-substrate: decreasing from 1.70(9)% at Y = 2 nm down to 0.47(2)% at Y = 30 nm;
- in-plane strain of 0.79(2)% in MSF10 and 0.59(2)% in MMF10.

HRSTEM results on the multilayers on MgO/STO can be summarized as follows:

- the dislocations are regularly distributed at the MgO/STO interface with an average separation of 2.8(8) nm and with an average distance of -0.2(6) nm from the interface,
- at the Fe/MgO interface, the dislocation average separation is 5.3(2.7) nm and the dislocations are distributed inside the Fe layer with an average distance of 0.95(71) nm from the interface.
- no dislocations were observed at the Fe/Cr or Cr/Fe interfaces.

8.1 Strains in MgO

In both MgO and Fe layers, we get a strain smaller than 1%, which agrees with the maximum values expected in metals [43,19,20] and oxides (dislocations are formed when the elastic energy stored in the strained layer is large enough to overcome the activation energy of formation of a new dislocation). Note that at the MgO/STO interface the dislocations are formed during the growth of MgO at 873 K. The expansion coefficients of MgO and STO are not equal so that the strain at the end of the preparation was different from that measured at room temperature. De Ligny and Richet [44] showed that the thermal linear expansion in STO has a constant value α_L=1.077(7) 10^{-5} K^{-1} up to 1800K. Data reported by Leroy [45] for MgO can be interpolated as α_L= (6.73 10^{-6} + 1.49 10^{-8} T - .402 10^{-12} T^2) K^{-1} between 300 and 900 K, and for Fe, data reported by [46] give α_L= (8.37 10^{-6}+7.25 10^{-9} T) K^{-1} between 300 and 1100 K.

The expansion coefficient of MgO is larger than that of STO above 300 K (Fig. A8a). For the MgO buffer layer, the compression strain thus decreases when decreasing the temperature after the growth (Fig. A8b). We can thus assume that the number of epitaxial dislocations does not vary during cooling. The residual strain of -0.37% at 300 K corresponds to a strain of -0.54% at 873 K. Dislocations had formed in the MgO buffer layer during growth until the strain was around 0.5% as expected in oxides. This corresponds to the strain limit corresponding to an elastic energy equal to the dislocation formation energy. Indeed, the residual strains deduced from x-ray diffraction and HRSTEM are equal for MgO.

The relaxation due to the dislocations observed in HRSTEM has been calculated considering that in MgO, an *fcc* system, the stable Burgers vector is of type ½<011> [42]. Calling the interface plane (100) and the beam direction [010], the glide plane is (100) and the edge

contribution of the Burgers vector in the image plane is ½[001]. Writing the coincidence between *n* planes of MgO and (*n*+1) planes of STO between two dislocations separated by *d*, we get:

$d = (n+1) \times a_{STO}/2 = n \times a_{MgO} \times (1+\varepsilon_{MgO}) / 2 \rightarrow n = a_{STO} / (a_{MgO} \times (1+\varepsilon_{MgO}) - a_{STO})$

$\rightarrow d = a_{MgO} \times (1+\varepsilon_{MgO}) /2 \times a_{STO} / (a_{MgO} \times (1+\varepsilon_{MgO}) - a_{STO})$

d = 2.685 nm for $\varepsilon_{MgO} = 0$ and d = 2.82(4) nm for ε_{MgO} = -0.37(11)% (from XRD).

The dislocation separation distance observed with HRSTEM is in very good agreement with the value deduced from XRD results.

8.2 Strains in first layer of Fe

The same calculation is done for Fe, considering the 45° rotation of the Fe lattice with respect to the MgO lattice. In Fe, a *bcc* system, the stable Burgers vectors are of ½<111> or <100> type, with a small energy difference [42]. If we call the interface plane (100) and the beam direction [0-11], the glide plane is (100) and the edge contribution of the Burgers vector ½[011] in the image plane for the <100>-type dislocations. Equivalent equations can be written:

$d = a_{MgO} \times (1+\varepsilon_{MgO}) \times a_{Fe} \times (1+\varepsilon_{Fe}) \times \sqrt{2} / (a_{MgO} \times (1+\varepsilon_{MgO}) - a_{Fe} \times (1+ \varepsilon_{Fe}) \times \sqrt{2}) / 2$

d =5.36 nm for $\varepsilon_{MgO} = \varepsilon_{Fe} = 0$ and 7.80(32) nm for ε_{MgO} and ε_{Fe} measured by XRD.

In the first Fe layer, the average separation of dislocations (5.3 ± 2.7 nm) is slightly smaller (Fig.10a) than the value expected considering the average residual strain in the Fe layers (7.8(3) nm) in multilayers. It is nevertheless within the error bars.

Fe is more ductile than MgO. This explains why the dislocations are formed after some Fe planes are grown on MgO. As in a Stranski-Krastanov growth mode, the first Fe layers grow coherently. When the elastic energy gets too high, dislocations are formed and slide towards the interface. This effect is much more rapid in oxides like MgO, which is why the dislocations are exactly at the MgO/STO interface.

We did not observe any dislocation with Burger's vector perpendicular to the interface as observed in [47]. The deposition of a 20nm-thick MgO buffer layer appears thus to be a better method to get rid of the surface steps and pollution than that used by the authors of [47]: etching in 85% o-phosphoric acid and exposure to an electron cyclotron resonance microwave plasma in the vacuum chamber. The high vacuum clean surface and the deposition of Fe at room temperature followed by an annealing, as used in this work, improves the interface and avoids the formation of dislocations that do not contribute to the lattice misfit relaxation at the interface.

8.3 *Y* variation of strain

The additional strain in Fe deposited on MgO/STO varies as 1/*Y*. Only the first Fe layer was annealed for 2h at 773 K after deposition at room temperature. All other sub-layers were deposited at room temperature and not annealed. The thermal strain has no reason to vary with Fe thickness. In addition, its sign would be negative as the expansion coefficient is smaller in STO than in Fe (Fig. A8).

A possible explanation of these observations would be that some strontium atoms segregate to the MgO surface during the MgO growth at 873 K. The diffusion of Sr through 20 nm of

MgO is possible at 873 K as deduced from the data of [48]. EELS spectra acquired in the most favourable conditions to observe Sr in MgO and Fe showed that the strontium concentration in the MgO layer and in the first Fe layer is smaller than the detection limit of about 1 at.%.

During Fe growth at room temperature, if an Sr layer either floated at the Fe surface or stayed at the Fe/MgO interface, these Sr atoms would interdiffuse inside the Fe layer during the 2 h 773 K annealing subsequent to the Fe growth, attaining a homogeneous distribution [48] and an Sr concentration varying as 1/*Y*. The increase in in-plane lattice parameter would thus correspond to a swelling of the first Fe layer due to the presence of Sr. Considering the calculated size factor of Sr in *bcc* Fe: *SF*=1.473 [50] we can estimate the amount of Sr from the additional strain in TSF*Y* compared to TMF*Y*. We find a third of a monolayer and an average concentration around 0.5%. This concentration is below the detection limit of EELS in our conditions. If Sr is present in the first Fe layer, it would behave as a buffer layer with a lattice parameter varying as 1/*Y* because a constant amount of Sr would be dissolved in a *Y*-thick film.

The other layers do not contain any Sr as they were grown at room temperature and were not annealed afterwards. They are slightly more strained in tension than if the swelling of the first Fe layer was not present. The swelling of the first Fe layer cannot be observed directly from the out-of-plane lattice parameter because only an average lattice parameter is measured and because the other Fe layers have a negative perpendicular strain associated with this in-plane positive strain.

9) Conclusion

In this paper, we have shown that using MBE enables to grow perfectly coherent Cr/Fe superlattices. The in-plane lattice parameters are equal in the Fe and Cr layers.

The residual in-plane strains are smaller than 0.5% in all trilayers and multilayers deposited on an MgO substrate. On an STO substrate, the residual in-plane strains are larger but remain smaller than 1% in trilayers with individual layers thicker than 5 nm, *i.e.* 35 monolayers. The additional strain has been attributed to a swelling of the first Fe layer which would be caused by a small contamination with Sr, present at the MgO surface at the end of the MgO growth. Sr atoms may diffuse inside the Fe first layer during its post-growth annealing.

In conclusion, these multilayers appear as good model systems to be used for diffusion coefficient measurements, because they contain very few defects at the interfaces. The strain difference notably enhances the XRD contrast to promote the interdiffusion kinetics studies in Fe-Cr systems using such superlattices. The swelling of the first Fe layer on STO could be used to prepare a buffer layer with finely accorded lattice parameter in future studies.

Acknowledgments:

Ms Wafaa Mohamed is thanked for her help in the thinning of samples for STEM; Dr Maylise Nastar is thanked for fruitful scientific discussions. Victor Dacosta and Benoit Gobaut for help in technical descriptions. This work was supported by the French National research agency (ANR-16-CE92-0002-02 MAGIKID), the EU ESTEEM3 grant agreement (No 823717) and the French Renatech NEEDS-Raisin program (CNRS-CEA-EDF-ANDRA-AREVA-IRSN-

BRGM). We acknowledge the XRD and TEM platforms of the IPCMS for the experimental support.

Appendices (or Supplementary material)

Appendix A: Some additional and more technical figures are given here to complete the main text.

Appendix B: Was the MgO buffer layer necessary to epitaxy the tri-layers?

To study the effect of the MgO buffer layer on the structure of the samples on MgO and on STO, we prepared Fe/Cr/Fe tri-layers on STO and MgO substrates with and without the MgO buffer layer. The thickness of each layer is 10 nm. $\theta/2\theta$ scans (Fig. A9) were realized on the tri-layers in the same conditions as those in Fig. 4.

On a trilayer grown on STO with no MgO buffer layer, the (200) Bragg peak of the tri-layer has a very low intensity. When an MgO buffer is grown first, the (200) Fe/Cr/Fe peak becomes extremely strong in comparison. The rocking curves (Fig. A10) are plotted with the same scale for measurements in the same conditions and clearly confirms the difference of epitaxial quality. This indicates that the MgO buffer layer is necessary to epitaxy Fe/Cr/Fe on STO substrate.

On MgO substrates, a good texture of the tri-layers is observed with and without the buffer layer with an epitaxial growth along [100] of MgO. The intensity of the (200) Bragg peak is nevertheless slightly higher for the TMF10 sample grown with a buffer layer than without a buffer layer indicating that the presence of MgO buffer layer reduces the substrate roughness in agreement with the AFM observations. The rocking curve is twice larger without MgO buffer layer, indicating an improve of the crystalline quality by the buffer layer. The out-of-plane and in-plane lattice parameters were calculated from XRD (same method as for Fig. 6) and the results are equivalent to those in TMF10.

Appendix C: Calculation of $\theta/2\theta$ intensity in multilayers

To calculate the intensity diffracted at a diffraction angle 2θ, we first need to calculate the complex amplitude. The complex diffusion length F_i of each individual atomic plane i is calculated: the phase is considered with reference to the surface plane called "1" (where the phase is 0). The phase is proportional to the position of the plane x_i calculated as the integrated distances $d_{i,i+1}$ (for (200) peak we have $d_{i,i+1}=a/2$): $\boldsymbol{x_1 = 0}$ and $\boldsymbol{x_i = \sum_{j<i} d_{i-1,i}}$ for $\boldsymbol{i > 1}$. The amplitude diffused by plane i is calculated considering the Fe-concentration of plane i: c_i. $F_i = F_{Fe}\, c_i + F_{Cr}\,(1-c_i)$. F_{Fe} and F_{Cr} are calculated as the complex sum of the Rayleigh and anomalous contributions: $\boldsymbol{F_i(s) = \sum_{\sigma=Fe,Cr} c_\sigma (f_\sigma + f_\sigma' + i f_\sigma'')}$. $\boldsymbol{f_m = \sum_{m=1}^{4} \alpha_{m,\sigma}\, e^{-\beta_{m,\sigma} s^2} + \gamma_\sigma}$ using $\boldsymbol{s = \sin\theta / \lambda}$, $F_i(s)$. Constants $\alpha_{m,\sigma}$, $\beta_{m,\sigma}$ and χ_σ are deduced from an Hartree-Fock calculation [51] for σ = Fe and Cr. The anomalous scattering coefficients f_m' and f_m'' are calculated in [52]. α_σ, β_σ, χ_σ, f_σ', and f_σ'' are given in Table A1 for Fe and Cr.

The intensity diffracted by the multilayer containing N planes is calculated from the diffracted amplitudes summed on each atomic plane: $I = A \cdot A^*$ with $A = \sum_{i=1,N} F_i\, e^{i\,4\pi s x_i}$.

The interplanar distance is assumed constant within the pure Fe and Cr layers. At the interfaces, the interplanar distance is assumed to be the average of those in the adjacent layers calculated from the Vegard's law calculated using the Fe and Cr lattice parameters and the local concentration.

Finally, a convolution was applied with a Gaussian (of width 0.23° adjusted on the Fe-buffer layers' XRD curves) to consider the global experimental resolution (due to the diffractometer and to the sample).

A least square fit is made varying the different variables: number of Fe planes in the first Fe layer, number of Cr planes in the Cr-layers, number of planes in the other Fe-layers, lattice parameter of Fe and of Cr. Due to the large number of variables, the least square fit is done using random values inside the possible intervals for each variable considering the parameters deduced from reflectometry and TEM. χ^2, the sum of the squared differences between experiment and simulation, is calculated for each set of variables and plotted as a function of each value. The interval is progressively reduced. About 70.000 calculations were usually necessary to obtain a clear minimum. Each variable value is finally deduced averaging the values corresponding to the 50 smallest χ^2 values. The curves shown in Fig.6 are simulated with the final value for each variable.

A python program was written to perform this minimization.

Table 1: Strains in MgO and Fe

Perpendicular strains $\varepsilon_{\perp}$ (from $\theta/2\theta$ for MgO and $\sin^2(\psi)$ for Fe) and in-plane strains $\varepsilon_{//}$ (from Poisson's law for MgO and $\sin^2(\psi)$ for Fe) in all layers.

Y (nm)	$\varepsilon_{\perp}$ (MgO) (%)	$\varepsilon_{//}$ (MgO) (%)	$\varepsilon_{\perp}$ (Fe) from $\sin^2(\psi)$ (%)	$\varepsilon_{//}$ (Fe) from $\sin^2(\psi)$ (%)	$\varepsilon_{\perp}$ (Fe) from $\sin^2(\psi)$ (%)	$\varepsilon_{//}$ (Fe) from $\sin^2(\psi)$ (%)
	TSF*Y*	TSF*Y*	TSF*Y*	TSF*Y*	TMF*Y*	TMF*Y*
2	0.146(02)	-0.338(26)	-2.14(35)	1.703(88)	-1.05(17)	0.786(40)
5	0.325(25)	-0.741(84)	-1.33(21)	1.099(42)	-0.54(8)	0.644(217)
10	0.195(24)	-0.450(86)	-0.90(16)	0.775(49)	-0.52(12)	0.394(49)
15	0.130(19)	-0.301(64)	-0.92(29)	0.796(35)	-0.82(13)	0.614(28)
20	0.292(29)	-0.675(112)	-0.49(10	0.465(37)	-0.51(13)	0.384(63)
25	0.202(24)	-0.466(87)	-0.60(11)	0.550(33)	-0.44(8)	0.329(28)
30	0.292(21)	-0.675(93)	-0.49(8)	0.466(21)	-0.50(13)	0.376(55)
	BSF*Y*	BSF*Y*	BSF*Y*	BSF*Y*	BMF*Y*	BMF*Y*
5	0.232(75)	-0.535(53)	-0.839(15)	0.937(68)	-0.336(28)	0.276(89)
10	0.156(89)	-0.359(20)	-0.874(5)	0.734(67)	-0.464(26)	0.416(113)
20	0.113(90)	-0.260(19)	-0.796(1)	0.575(46)	-0.613(15)	0.469(46)
	MSF10	MSF10	MSF10	MSF10	MMF10	MMF10
10	0.120(61)	-0.277(84)	-1.000(9)	0.788(23)	-0.809(8)	0.593(14)

Table A1: Constants to calculate scattering coefficients in Fe and Cr

Constants $\alpha_{m,\sigma}$, $\beta_{m,\sigma}$ and χ_{σ} deduced from an Hartree-Fock calculation [51] for σ = Fe and Cr. Anomalous scattering coefficients f_{σ}' and f_{σ}'' calculated in [52].

Element	χ	α_1	α_2	α_3	α_4	β_1	β_2	β_3	β_4	$-f'$	f''
Fe	1.037	11.769	7.357	3.522	2.305	4.761	0.307	15.354	76.881	1.11847	3.14837
Cr	1.183	10.641	7.354	3.324	1.492	6.104	0.392	20.263	98.74	0.25046	2.54513

References:

[1] I. Cook, *Materials research for fusion energy,* Nature Mater. **5** (2006) 77-80. https://doi.org/10.1038/nmat1584 .

[2] R.L. Klueh and A.T. Nelson, *Ferritic/martensitic steels for next-generation reactors,* J. Nucl. Mater., 371 (2007) 37-52. https://doi.org/10.1016/j.jnucmat.2007.05.005 .

[3] S. Zinkle and J.T. Busby, *Structural materials for fission and fusion energy*, Mater. Today 12 (2009) 12-19. https://doi.org/10.1016/S1369-7021(09)70294-9 .

[4] R. Herschberg, C.C. Fu, M. Nastar, and F. Soisson, *Atomistic modelling of the diffusion of C in Fe-Cr alloys,* Acta Mater. **165,** 638-653 (2019). https://doi.org/10.1016/j.actamat.2018.11.025 .

[5] E. Martinez, C.C. Fu, M. Levesque, M. Nastar, and F. Soisson, *Simulations of decomposition kinetics of Fe-Cr solid solutions during thermal aging,* Solid-Solid Phase Transformations In Inorganic Materials Pts 1-2, Solid State Phenomena International Conference on Solid-Solid Phase Transformations in Inorganic Materials (PTM 2010) June 6-11 2010, Avignon France, **172-174,**1016 (2011). https://10.4028/www.scientific.net/SSP.172-174.1016.

[6] E. Martinez, O. Senninger, C.C. Fu, and F. Soisson, *Decomposition kinetics of Fe-Cr solid solutions during thermal aging,* Phys. Rev. B **86,** 224109 (2012). https://10.1103/PhysRevB.86.224109 .

[7] M. Levesque, E. Martinez, C.C. Fu, M. Nastar, and F. Soisson, *Simple concentration-dependent pair interaction model for large-scale simulations of Fe-Cr alloys,* Phys. Rev. B **84,** 184205 (2011). https://10.1103/PhysRevB.84.184205 .

[8] M. Hennion, *Chemical SRO effects in ferromagnetic Fe alloys in relation to electronic band structure, J. Phys. F: Met. Phys.* **13** (1983) 2351-2358. https://doi.org/10.1088/0305-4608/13/11/017.

[9] I. Mirebeau, M. Hennion, and G. Parette, *First Measurement of Short-Range-Order Inversion as a Function of Concentration in a Transition Alloy,* Phys. Rev. Lett. **53** (1984) 687-690. https://doi.org/10.1088/0305-4608/13/11/017.

[10] I. Mirebeau and G. Parette, *Neutron study of the short-range order inversion in* $Fe_{1-x}Cr_x$, Phys. Rev. B **82** (2010) 104203. https://doi.org/10.1103/PhysRevB.82.104203 .

[11] I. Mirebeau, V. Pierron-Bohnes, C. Decorse, E. Rivière, C.C. Fu, Kangming Li, and G. Parette, N. Martin, *Magnetic and atomic short range order in* $Fe_{1-x}Cr_x$ *alloys,* Phys. Rev. B **100**, 224406 (2019), https://doi.org/10.1103/PhysRevB.100.224406.

[12] T.P.C. Klaver, R. Drautz, and M.W. Finnis, *Magnetism and thermodynamics of defect-free Fe-Cr alloys,* Phys. Rev. B 74, 094435 (2006). https://doi.org/10.1103/PhysRevB.74.094435 .

[13] P. Grünberg, R. Schreiber, Y. Pang, M. B. Brodsky, and H. Sowers, *Layered magnetic-structures - evidence for antiferromagnetic coupling of Fe layers across Cr interlayers*, Phys. Rev. Lett. **57** (1986) 2442. https://doi.org/10.1103/PhysRevLett.57.2442 .

[14] M.N. Baibich, J. M. Broto, A. Fert, F. Nguyen Van Dau, F. Petroff, P. Etienne, G. Creuzet, A. Friederich, and J. Chazelas, *Giant Magnetoresistance of (001)Fe/(001)Cr Magnetic*

Superlattices, Phys. Rev. Lett. **61** (1988) 2472-2475, https://doi.org/10.1103/PhysRevLett.61.2472 .

[15] S. S. P. Parkin and B. R. York, Appl. Phys. Lett. 62 (1993) 1842, *Influence of deposition temperature on giant magnetoresistance of Fe/Cr multilayers.* https://doi.org/10.1063/1.109542 .

[16] X. Bian, H.T. Hardner, and S.S.P. Parkin, *Investigation of magnetic coupling in sputtered epitaxial Fe/Cr and Co/Cu wedged structures*, J. Appl. Phys. **79** (1996) 4980-4982. https://doi.org/10.1063/1.361610 .

[17] E.E. Fullerton, M.J. Conover, J.E. Mattson, C.H. Sowers, and S.D. Bader, *Oscillatory interlayer coupling and giant magnetoresistance in epitaxial Fe/Cr(211) and (100) superlattices*, Phys. Rev. B **48** (1993) 15755. https://doi.org/10.1103/PhysRevB.48.15755 .

[18] When growing a layer on a substrate with a different lattice parameter, there is always a small residual strain, below 1%, with the same sign as the initial misfit [19-21]. As a_{MgO} = 0.42112 nm > a_{Fe}^{bulk} = 0.4057/$\sqrt{2}$ nm > a_{STO} = 0.3905 nm, the lattice parameter of a layer of MgO in epitaxy on STO will be a little smaller (we indeed measured an average residual strain of -0.37% in the MgO buffer) inducing a smaller lattice mismatch between Fe and the buffer layer on STO (-3.31% assuming that the surface lattice parameter of MgO is equal to the average lattice parameter) than between Fe and an MgO substrate (-3.66%).

[19] J.W. Matthews and J.L. Crawford, *Accommodation of misfit between single-crystal films of nickel and copper.* Thin Solid Films ***5*** (1970) 187-198. https://doi.org/10.1016/0040-6090(70)90076-3 .

[20] J.W. Matthews, 1975, *Epitaxial Growth* (Academic Press, New York)

[21] U. Gradmann, 1993, *Magnetism in ultrathin transition metal films*, in "Handbook of Magnetic Materials" (Ed. K.H.J. Buschow, Elsevier)

[22] D. Blavette, B. Deconihout, A. Bostel, J. M. Sarrau, M. Bouet, and A. Menand, *The tomographic Atom-Probe - A quantitative 3-Dimensional Nanoanalytical instrument on an atomic-scale*, *Rev. Sci. Instr.*, **64** (1993) 2911-2919. https://doi.org/10.1063/1.1144382 .

[23] E.J. Kirkland, R.F. Loane, and J. Silcox, *Simulation of annular dark field stem images using a modified multislice method*, Ultramicroscopy **23** (1987) 77-96. https://doi.org/10.1016/0304-3991(87)90229-4 .

[24] S.J. Pennycook, *Z-contrast STEM for materials science*, Ultramicroscopy **30** (1989) 58-69. https://doi.org/10.1016/0304-3991(89)90173-3 .

[25] R.F. Egerton, (2011), *Physics of Electron Scattering*. In: Electron Energy-Loss Spectroscopy in the Electron Microscope. Springer, Boston, MA. https://doi.org/10.1007/978-1-4419-9583-4_3 .

[26] Hyperspy.org ; doi/10.5281/zenodo.592838.svg

[27] F. de la Peña, M.H. Berger, J.F. Hochepied, F. Dynys, O. Stephan, and M. Walls, *Mapping titanium and tin oxide phases using EELS: An application of independent component analysis*, Ultramicroscopy **111** 169 (2011). https://doi.org/10.1016/j.ultramic.2010.10.001 .

[28] G.R. Harp and S.S.P. Parkin, *Epitaxial growth of metals by sputter deposition*, Thin Solid Films **288** (1996) 315. https://doi.org/10.1016/S0040-6090(96)08808-6.

[29] We observe islands that are 4-5 nm high, i.e. about 15 atomic layers thick. They were later covered by the MgO buffer layer. We could not characterize the composition of these islands as scanning electron microscopy or atomic probe analysis are not possible due to charging effects because MgO is an electric insulator. In TEM we did not observe any measurable C contamination of the Fe/MgO interface nor inside the MgO substrate.

[30] N. Najjari, D. Halley, M. Bowen, H. Majjad, Y. Henry, and B. Doudin, *Electrical switching in Fe/V/MgO/Fe tunnel junctions,* Phys. Rev. B. 81 (2010) 174425. https://doi.org/10.1103/PhysRevB.81.174425.

[31] D. Halley, O. Bengone, S. Boukari, and W. Weber, *Novel oscillation period of the interlayer exchange coupling in Fe/Cr/Fe due to MgO capping*, Phys. Rev. Lett. **102**, 027201 (2009). https://doi.org/10.1103/PhysRevLett.102.027201 .

[32] J. Solano, O. Gladii, P. Kuntz, Y. Henry, D. Halley, and M. Bailleul, *Spin-wave study of magnetic perpendicular surface anisotropy in single crystalline MgO/Fe/MgO films,* Phys. Rev. Materials **6** 124409 (2022). https://doi.org/10.1103/PhysRevMaterials.6.124409 .

[33] F. Vurpillot, D. Larson, and A. Cerezo, *Improvement of multilayer analyses with a three-dimensional atom probe*, Surf. Interface Anal. **36** (2004) 552–558. https://doi.org/10.1002/sia.1697 .

[34] The order of magnitude of a monolayer formation time in a 6.10^{-7} Pa vacuum is 530 s with a sticking coefficient of 1, which is the case for O encountering a Cr surface (see for example https://physics.ucf.edu/~btonner/XRAY/Courses/Phy904/Vacuum/Vacuum.htm). Moreover, as some MgO has been evaporated in a previous step, the residual atmosphere is undoubtedly rich in O.

[35] This relationship indicates that the in-plane [011] direction of the (100) plane (film surface) is aligned on the [010] direction of the (100) substrate surface plane.

[36] E.E. Fullerton, M.J. Conover, J.E. Mattson, C.H. Sowers, and S.D. Bader, *Orientationally independent antiferromagnetic coupling in epitaxial Fe/Cr (211) and (100) superlattices,* J. Appl. Phys. **75** (1998) 6461. https://doi.org/10.1063/1.356962 .

[37] A.A.R. Fernandes, C.A. Ramos, A. Macedo Teixeira, and E.E. Fullerton, *Magnetization temperature dependence in Fe/Cr superlattices,* Physica B **320** (2002) 175–177. https://doi.org/10.1016/S0921-4526(02)00668-3 .

[38] The size factor *SF* is the limit of relative volume increase when adding 1% of impurity atoms for large atom numbers in the crystal: $\Delta V/V=3\ \Delta l/l = SF \cdot c$ with c in percent.

[39] E. Akkshaya Devi, R. Chinnappan, and C.S. Sudar, *First-principles study of interaction energies of atomic defects in bcc ferromagnetic iron,* Phys. Rev. B 98, 144104 (2018). https://doi.org/10.1103/PhysRevB.98.144104 .

[40] D. Sander, *The correlation between mechanical stress and magnetic anisotropy in ultrathin films, Rep. Prog. Phys.* **62** (1999) 809. https://doi.org/10.1088/0034-4885/62/5/204.

[41] C.S. Zha, H.K. Mao, and R.J. Hemley, *Elasticity of MgO and a primary pressure scale to 55 GPa,* PNAS **97** (2000) 13494-13499. https://doi.org/10.1073/pnas.240466697.

[42] J.P. Hirth and J. Lothe, *Theory of Dislocations,* 1992, Krieger Publishing Company

[43] W.A. Jesser and J.W. Matthews, *Evidence for pseudomorphic growth of iron on copper,* Phil. Mag. **15** (1967) 1097-1106. https://doi.org/10.1080/14786436708222752 .

[44] D. de Ligny and P. Richet, *High-temperature heat capacity and thermal expansion of $SrTiO_3$ and $SrZrO_3$ perovskites.* Phys. Rev. B **53** (1996) 3013-3022. https://doi.org/10.1103/PhysRevB.53.3013 .

[45] M. A. Leroy, *Films minces épitaxiés de chrome pour l'électronique de spin: propriétés de volume et d'interface,* PhD thesis, Univ. Lorraine, France, (2013), interpolation of Fig. 11.5 p. 105, http://docnum.univ-lorraine.fr/public/DDOC_T_2013_0181_LEROY.pdf.

[46] W.B. Pearson, in" A Handbook of lattice spacings and structures of metals and alloys", Pergamon Press, London, 1958, vol. 4. eBook ISBN: 9781483226613.

[47] J.L. Du, H.Q. Chen, C. Xu, Y. Fan, Y.H. Qiu, H. Wang, and E.G. Fu, *Stress of misfit dislocation at Fe/MgO interface drives the annihilation of radiation induced defects*, Acta Mater. **210** (2021) 116798. https://doi.org/10.1016/j.actamat.2021.116798 .

[48] I. Sakaguchi, H. Yurimoto, and S. Sueno, *Strontium and Silicon Simultaneous Diffusion in Single-Crystal MgO, J.* Am. Ceram. Soc. *75*, 3477-80 (1992). https://doi.org/10.1111/j.1151-2916.1992.tb04454.x.

[49] C. D. Versteylen, N. H. van Dijk, and M. H. F. Sluiter, *First-principles analysis of solute diffusion in dilute bcc Fe-X alloys***,** Phys. Rev. B **96** (2017) 094105. https://doi.org/10.1103/PhysRevB.96.094105 .

[50] J. Hepburn, E. MacLeod, and G. J. Ackland, *Transition metal solute interactions with point defects in fcc iron from first principles*, Phys. Rev. B **92** (2015) 014110. https://doi.org/10.1103/PhysRevB.92.014110 .

[51] http://lampx.tugraz.at/~hadley/ss1/crystaldiffraction/atomicformfactors/formfactors.php

[52] http://skuld.bmsc.washington.edu/scatter/AS_periodic.html

Figure captions:

Figure 1: AFM images on the degassed substrate (a,c) and the MgO buffer layer (b,d) on the MgO (a,b) and STO (c,d) substrates. The sizes of the squares are 10 µm x 10 µm. The height scale is indicated on the right of the figures. Below each image are plotted the profiles along the lines. The average roughness (RMS) and average height on maximums of the roughness (rmh) are indicated below each plot.

Figure 2: MSF10: (a) BF-STEM image in cross-section. (b) 3D reconstruction from APT around the 4 top Cr layers. (c) from top to bottom: maps of O from a 7*7*60 nm^3 box extracted close to the (100) pole (black rectangle in (b)); idem for Fe and Cr; the relative atomic composition of Fe, Cr and O (colour online) along the growth direction (scale on the right for O), (d) HAADF and EELS maps on Ti, O, Fe, and Cr (colour online) from EELS.

Figure 3: Some examples of reflectometry measurements (colour online) and fits with the densities ρ (in g/cm^3: ρ_{STO}=5.12, ρ_{MgO}=3.58, ρ_{Fe}=7.8, ρ_{Au}=19.3) and the following thicknesses (d in nm) and RMS roughness (σ in nm): BSF5: d_{MgO}=19.02, d_{Fe}=4.66, d_{Au}=9.75, σ_{MgO}=0.26, σ_{Fe}=0.19, σ_{Au}=0.22; TSF30: d_{MgO}=19.97, $d_{Fe/Cr}$=83.61, d_{Au}=4.76, σ_{STO}=0.21, σ_{MgO}=0.3, σ_{Fe}=0.24, σ_{Au}=0.21. In inset: zoom showing the oscillations due to the (Fe/Cr/Fe) thickness.

Figure 4: Global high-angle $\theta/2\theta$ scans of B*X*F*Y* buffer layers, T*X*F*Y* tri-layers and M*X*F10 multilayers for the *X*=S (STO substrate; (a)) and M (MgO substrate; (b)). The sample names are indicated in the margin (thicknesses *Y* from the bottom to the top: 2, 5, 10, 15, 20, 25, and 30 nm for T*X*F*Y*, 10 and 20 nm for BMF*Y*, 5, 10, and 20 nm for BSF*Y*; M*X*F10 are the topmost curves, in blue online). The curves are shifted for clarity. (*h*00) peaks are located at 22.9°, 46.4°, 72.5°, 104.3° for STO with *h*=1 to 4; MgO peaks are located at 42.9° and 94.1°

with *h*=2 and 4; Au peaks are located at 44.4° and 98.2° with *h*=2 and 4, whereas the Fe-Cr peak is located around 65.5° with *h*=2.

Figure 5: (a) High resolution TEM image and (b) diffraction on BSF20.

Figure 6: XRD normalized intensity (linear scale) of the Fe/Cr (200) peak in the trilayers and multilayers ($\theta/2\theta$ scans). The experimental intensities are plotted as bullets and the simulations as lines. (a,b) Measured and simulated intensities in trilayers (TMF*Y* and TSF*Y* respectively). (c,d): Measured (bullets) and simulated (lines) intensities in MMF10 and MSF10 multilayers respectively (amplified intensities, x10 in MMF10 and x100 in MSF10, as circles). The names of the different satellites are given in (d).

Figure 7: $\sin^2(\psi)$ plots of the lattice parameters for Fe, Cr in (a) B*X*F*Y*, (b) TMF*Y*, (c) M*X*F10, and (d) TSF*Y*. In TMF2, TMF5, and TSF2, only the average lattice parameters could be determined. (b) and (d) curves are split for more clarity in Figs. A6 and A7. The symbols are:

in (a): BMF5 ▲, BMF10 ■, BMF20 ●, BSF5 △, BSF10 □, BSF20 ○;

in (b) and (d): T*X*F2 □, T*X*F5 ○ , T*X*F10 ▷, T*X*F15 △, T*X*F20 ◇, T*X*F25 ◁, T*X*F30 ▽;

in (c): the different satellites are S_{-1} ▲, S_0 ■, S_1 ▼; full (black online) symbols correspond to MMF10 and open (red online) symbols to MSF10; $a_\perp$ and $a_{//}$ are indicated at $\sin^2(\psi) = 0$ and 1 respectively, with ✳ in MMF10 and × in MSF10.

Figure 8: Residual in-plane strains from $\sin^2(\psi)$ plots for Fe and MgO in BSF*Y*, TSF*Y*, and TMF*Y*. The weighted averages and error bars of in-plane strains in Fe for TMF*Y* (0.45 ± 0.13%) and in MgO for TSF*Y* (-0.37 ± 0.11%) are shown as horizontal hatched bars. The continuous

line (blue online) corresponds to (0.45 + 2.85/*Y*)%: the 1/*Y* fit of the departure of $\varepsilon_{//}$(Fe) on STO from the average of $\varepsilon_{//}$(Fe) on MgO (0.45%).

Figure 9: Examples of HRSTEM images: raw data (a,d) and data treated to evidence misfit dislocations (b,e) at the MgO/STO (a,b) and Fe/MgO (d,e) interfaces in the MSF10 multilayer. Raw images (a,d) were Fourier transformed (c,g), filtered applying a mask on the 020 (resp. 011) in-plane peak of MgO and STO (resp. Fe) (circled on the horizontal axis on (c,g), green online), and inverse Fourier transformed to image the atomic planes and evidence the epitaxy dislocations (b,e). The wavy (blue online) lines show the approximate location of the interfaces. In black (red online) are the dislocations due to interfacial strain relaxation and in grey (yellow online) are what appear to be pairs of opposite dislocations that are in fact due to artefacts. The dislocations located between the long black – red online – arrows are counted in 5 (resp. 7) similar images. We also imaged in (f) the component of dislocations with the Burger's vector perpendicular to the interface with a mask on the (200) peaks of Fe and MgO (circled in (g) on the vertical axis – magenta online). We observe that there is no such component associated to the misfit dislocations. The latter have thus *b*=1/2 [002] (projected on the image as ½[011]), and not *b*=½[111] (with the same projection).

Figure 10: (a) Distribution of distances between neighbour dislocations at both interfaces (narrow dark bars – blue online: MgO/STO; wide light bars – beige online: Fe/MgO) and the corresponding averages. The different lines show the expected values in the cases: MgO/STO interface (long lines): on the left in black: ε_{MgO}=0; on the right in grey (green online): ε_{MgO}=-0.4%. Idem at Fe/MgO interface (short lines): on the left (blue online): ε_{MgO}=ε_{Fe}= 0; center (red online): ε_{MgO}=-0.4%, ε_{Fe}=0; on the right (pink online): ε_{MgO}=-0.4%, ε_{Fe}=0.8% (MSF10). (b)

Average strains deduced from STEM in each sample (●: MgO/STO interface; ▲: Fe/MgO interface; the mean values and the standard deviations are indicated as hatched bars) compared to the strains deduced from XRD on MgO in MSF10 (□) and on Fe in MMF10 (star – violet online) and MSF10 (▽). (c) Distribution of distances of individual dislocations from the interface: in narrow bars (blue online) at MgO/STO interface, in wide bars (beige online) at Fe/MgO interface.

Figure A1: RHEED patterns of the first-deposited Fe layer before (a) and after annealing (b), of the Cr layer (c) and the second Fe layer (d) deposited at 300K. The substrate is MgO in the left panel (azimuth [100] in (a,b) and [110] in (c,d)) and STO in the right panel (azimuth [100] in (a,b,d) and [110] in (c)).

Figure A2: Characteristics deduced from the fits of the $\theta/2\theta$ x-ray diffraction scans: (a) Rocking curves full widths; (b) Coherence length deduced from the width of the two main peaks in B*X*F*Y* and T*X*F*Y* (pink online dot-dashed line: expected total thickness; claret online dashed line: expected thickness of the bilayer from reflectometry $2e_R/3$; green online dotted line: expected individual thickness $e_R/3$). (c,d) Individual thicknesses in the Cr and Fe layers in the two kind of fits ($e_3=e_1$; $e_3>e_1$); (e,f) out-of-plane lattice parameters in the two types of fits ($e_3=e_1$; $e_3>e_1$) in Cr and Fe layers of trilayers and in multilayers.

Figure A3: Pole figures: to determine all the orientations of *(hkl)* planes present in the sample. The pole figure method consists in fixing the diffraction angle θ to the value corresponding to the d_{hkl} inter-reticular distance and collecting the diffracted intensity at

different ϕ (0°< ϕ < 360°) and χ (0°< χ < 90°) angles, where ϕ is the rotation angle of the sample around its normal and χ the tilt angle of the sample perpendicularly to the diffraction plane. An epitaxial layer gives intense and narrow *(hkl)* spots at specific ϕ and χ angles corresponding to the symmetry of the crystal. If the growth is only textured (all the crystals have the same growth direction but no common direction in the sample plane), a ring is observed at a specific χ. If the growth is polycrystalline, the intensity is spread across the whole solid angle. (a) Definition of angles. (b) How to read the stereographic projection plots of a quarter pole figure. (c) Maximum intensity of the (011) peak as a function of *Y*. (d) Pole figures in TSF2 (the (020) peak of STO is located at 4° from the ϕ = 90° direction). (e) Pole figure in TSF25 (the intensity is multiplied by 45 in the two light squares to make the (200) peak of the substrate visible).

Figure A4: Simulations of the $\theta/2\theta$ x-ray diffraction scans in MMF10 in $\log_{10}$ plot. Circles: experimental points. Red online continuous lines: simulation with diffraction length and perpendicular-strain contrasts. Blue online dotted lines: simulation with diffraction length contrast only. The light colours correspond to similar simulations including a 0.002 I_{MAX} background. Architecture of the superlattice: $(Cr_{70}/Fe_{64})_5/Fe_{46}$ (the subscripts are the N_i's). Parameters of the simulations: a_{Fe}=0.28452 nm, a_{Cr}=0.28857 nm for the continuous lines; a_{Fe}=a_{Cr}=0.2866 nm for the dotted lines.

Figure A5: Examples of maps in reciprocal space in the MMF10 sample: (a) (200) peak (ψ = 0°), (b) (211) peak ($\psi \approx$ 34°), (c) (222) peak ($\psi \approx$ 55°), and (d) (130) peak ($\psi \approx$ 72°). (a,b) were measured varying ω; (c,d) were measured varying ψ.

Figure A6: $\sin^2(\psi)$ plots of the lattice parameters for Fe, Cr in TMF*Y* (same data and symbols as Fig. 7b split for clarity). The error bars are shown inside the symbols.

Figure A7: $\sin^2(\psi)$ plots of the lattice parameters for Fe, Cr in TSF*Y* (same data and symbols as Fig. 7d split for clarity). The error bars are shown inside the symbols.

Figure A8: (a) Thermal expansion coefficients, α_L, of bulk STO, MgO, Fe, and Cr between 300 K and 900 K. (b) Lattice parameter normalized to its value at 773 K in bulk STO, MgO, Fe, and Cr between 300 K and 900 K deduced from α_L by integration after interpolating α_L with the second-degree polynomial function (the hatched range containing the Néel temperature of Cr was discarded).

Figure A9: $\theta/2\theta$ curves for T*X*F10 samples deposited without and with the MgO buffer layer on MgO (left panel) and STO (right panel).

Figure A10: $\boldsymbol{\omega}$ scans for T*X*F10 samples without and with the MgO buffer layer on MgO (left panel) and STO (right panel).

Table captions:

Table 1: Strains in MgO and Fe

Perpendicular strains $\varepsilon_\perp$ (from $\theta/2\theta$ for MgO and $\sin^2(\psi)$ for Fe) and in-plane strains $\varepsilon_{//}$ (from Poisson's law for MgO and $\sin^2(\psi)$ for Fe) in all layers.

Table A1: Constants to calculate scattering coefficients in Fe and Cr

Constants $\alpha_{m,\sigma}$, $\beta_{m,\sigma}$ and χ_σ deduced from an Hartree-Fock calculation [51] for σ = Fe and Cr. Anomalous scattering coefficients f_σ' and f_σ" calculated in [52].

Highlights

- Coherent Cr/Fe superlattices grown using MBE with an MgO buffer layer on MgO or $SrTiO_3$
- Film structure (strain and stress) different on $MgO_{20nm}/SrTiO_3$ and MgO substrates
- XRD contrast in Fe/Cr superlattices notably enhanced by Fe *vs* Cr strain difference

Table 1: Strains in MgO and Fe

Perpendicular strains $\varepsilon_{\perp}$ (from $\theta/2\theta$ for MgO and $\sin^2(\psi)$ for Fe) and in-plane strains $\varepsilon_{//}$ (from Poisson's law for MgO and $\sin^2(\psi)$ for Fe) in all layers.

Y (nm)	$\varepsilon_{\perp}$ (MgO) (%)	$\varepsilon_{//}$ (MgO) (%)	$\varepsilon_{\perp}$ (Fe) from $\sin^2(\psi)$ (%)	$\varepsilon_{//}$ (Fe) from $\sin^2(\psi)$ (%)		$\varepsilon_{\perp}$ (Fe) from $\sin^2(\psi)$ (%)	$\varepsilon_{//}$ (Fe) from $\sin^2(\psi)$ (%)
	TSF*Y*	TSF*Y*	TSF*Y*	TSF*Y*		TMF*Y*	TMF*Y*
2	0.146(02)	-0.338(26)	-2.14(35)	1.703(88)		-1.05(17)	0.786(40)
5	0.325(25)	-0.741(84)	-1.33(21)	1.099(42)		-0.54(8)	0.644(217)
10	0.195(24)	-0.450(86)	-0.90(16)	0.775(49)		-0.52(12)	0.394(49)
15	0.130(19)	-0.301(64)	-0.92(29)	0.796(35)		-0.82(13)	0.614(28)
20	0.292(29)	-0.675(112)	-0.49(10	0.465(37)		-0.51(13)	0.384(63)
25	0.202(24)	-0.466(87)	-0.60(11)	0.550(33)		-0.44(8)	0.329(28)
30	0.292(21)	-0.675(93)	-0.49(8)	0.466(21)		-0.50(13)	0.376(55)
	BSF*Y*	BSF*Y*	BSF*Y*	BSF*Y*		BMF*Y*	BMF*Y*
5	0.232(75)	-0.535(53)	-0.839(15)	0.937(68)		-0.336(28)	0.276(89)
10	0.156(89)	-0.359(20)	-0.874(5)	0.734(67)		-0.464(26)	0.416(113)
20	0.113(90)	-0.260(19)	-0.796(1)	0.575(46)		-0.613(15)	0.469(46)
	MSF10	MSF10	MSF10	MSF10		MMF10	MMF10
10	0.120(61)	-0.277(84)	-1.000(9)	0.788(23)		-0.809(8)	0.593(14)

Table A1: Constants to calculate scattering coefficients in Fe and Cr

Constants $\alpha_{m,\sigma}$, $\beta_{m,\sigma}$ and χ_{σ} deduced from an Hartree-Fock calculation [51] for σ = Fe and Cr. Anomalous scattering coefficients f_{σ}' and f_{σ}" calculated in [52].

Element	χ	α_1	α_2	α_3	α_4	β_1	β_2	β_3	β_4	$-f'$	f''
Fe	1.037	11.769	7.357	3.522	2.305	4.761	0.307	15.354	76.881	1.11847	3.14837
Cr	1.183	10.641	7.354	3.324	1.492	6.104	0.392	20.263	98.74	0.25046	2.54513

Figure 1

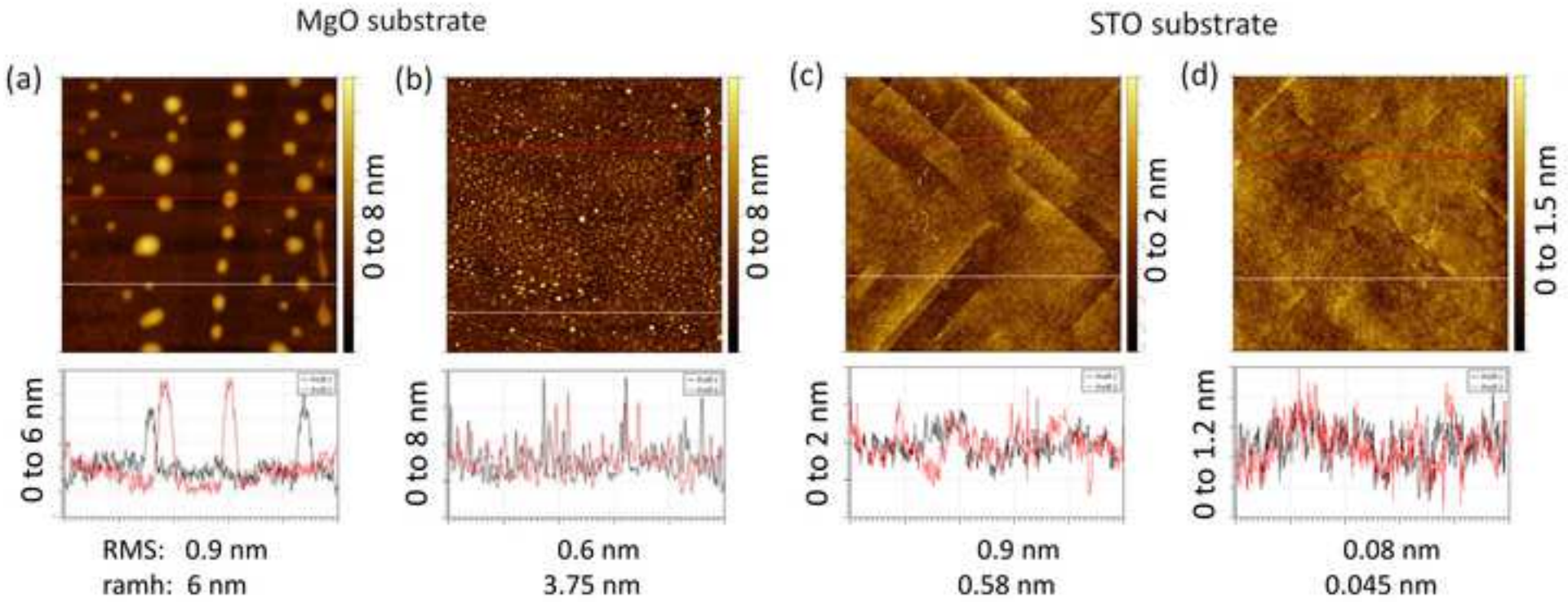

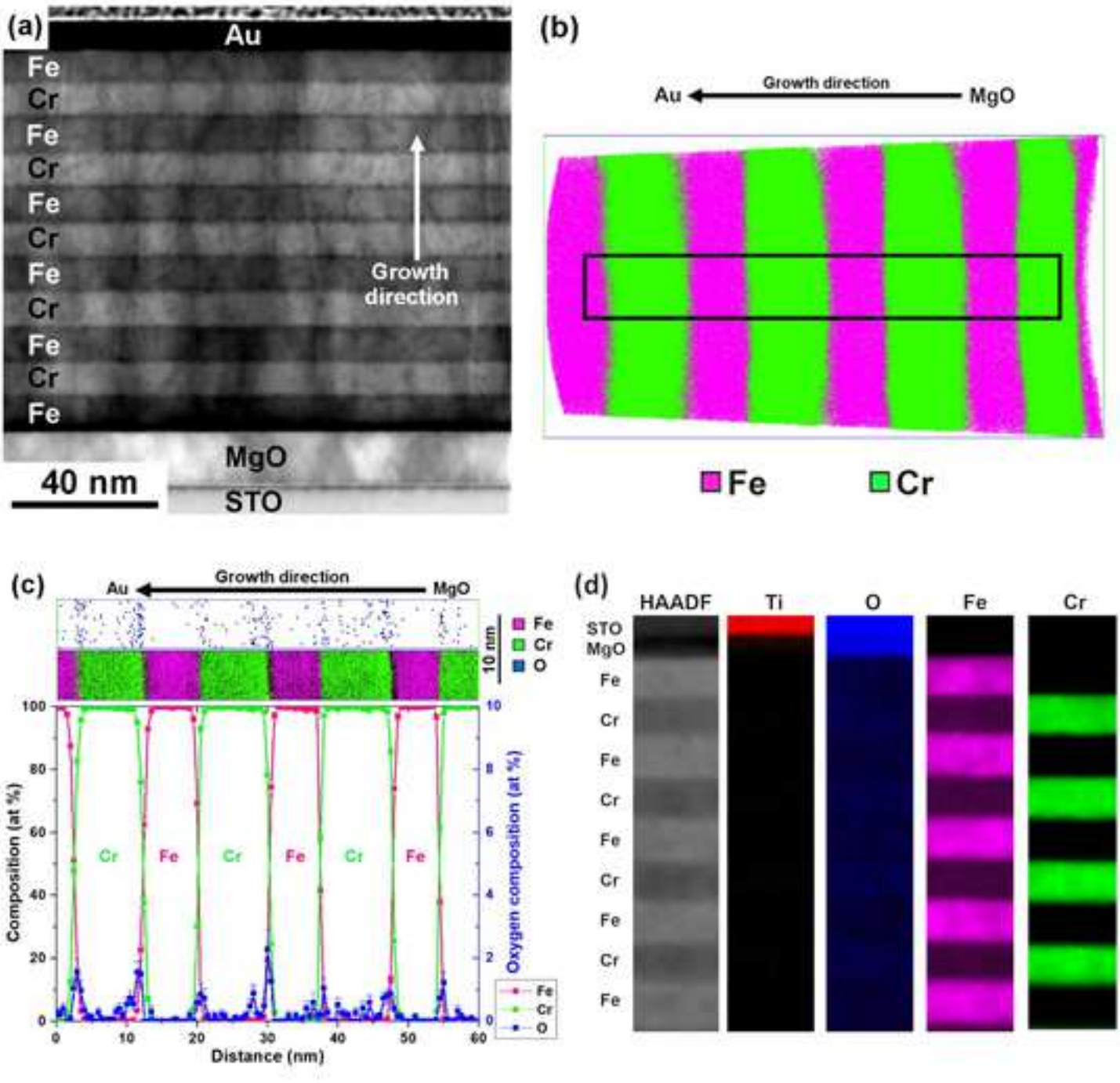

Figure 3

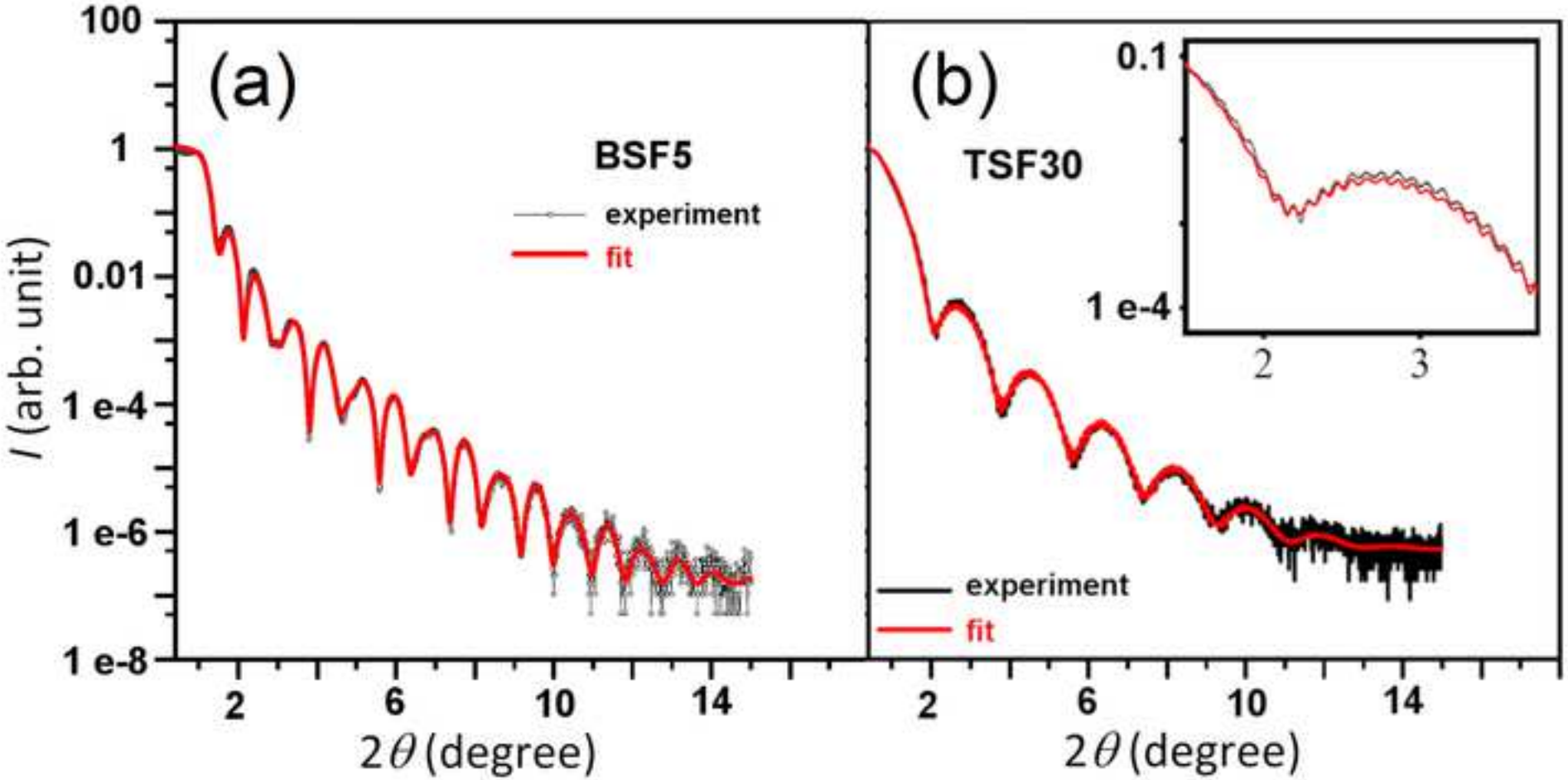

Figure 4a

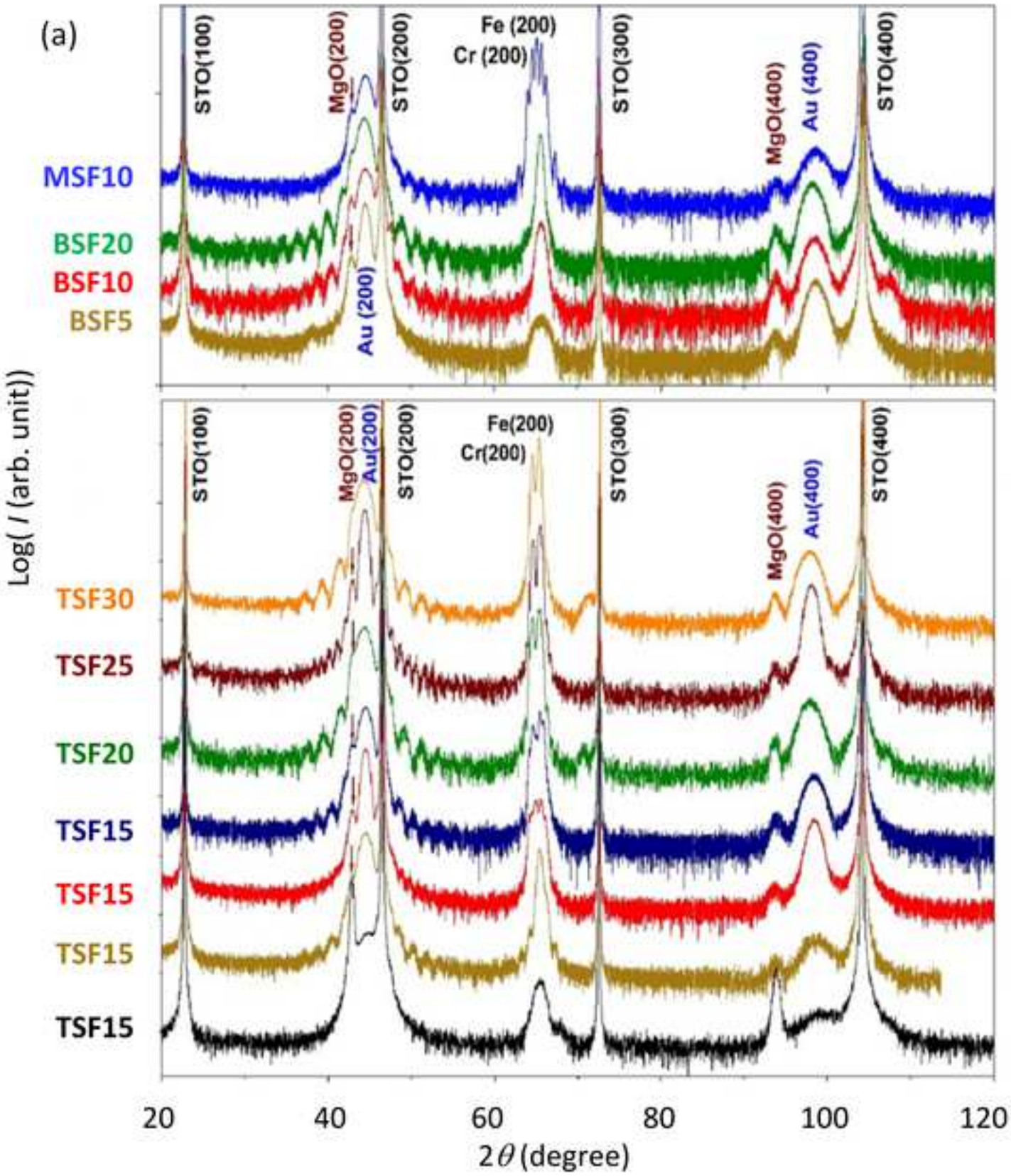

Figure 4b

Click here to access/download;Figures (if any);Fig4b_se1.jpg

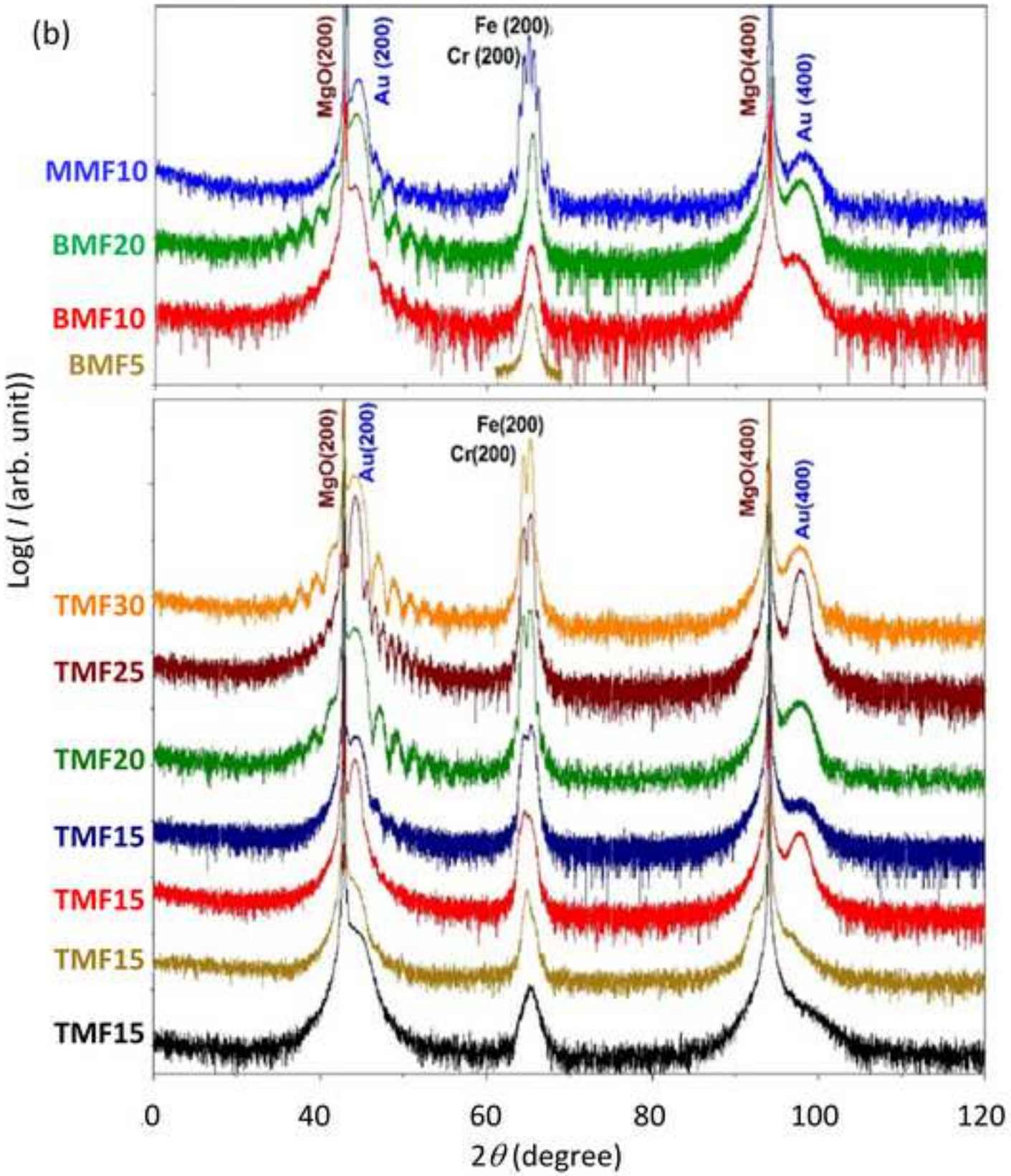

Figure 5

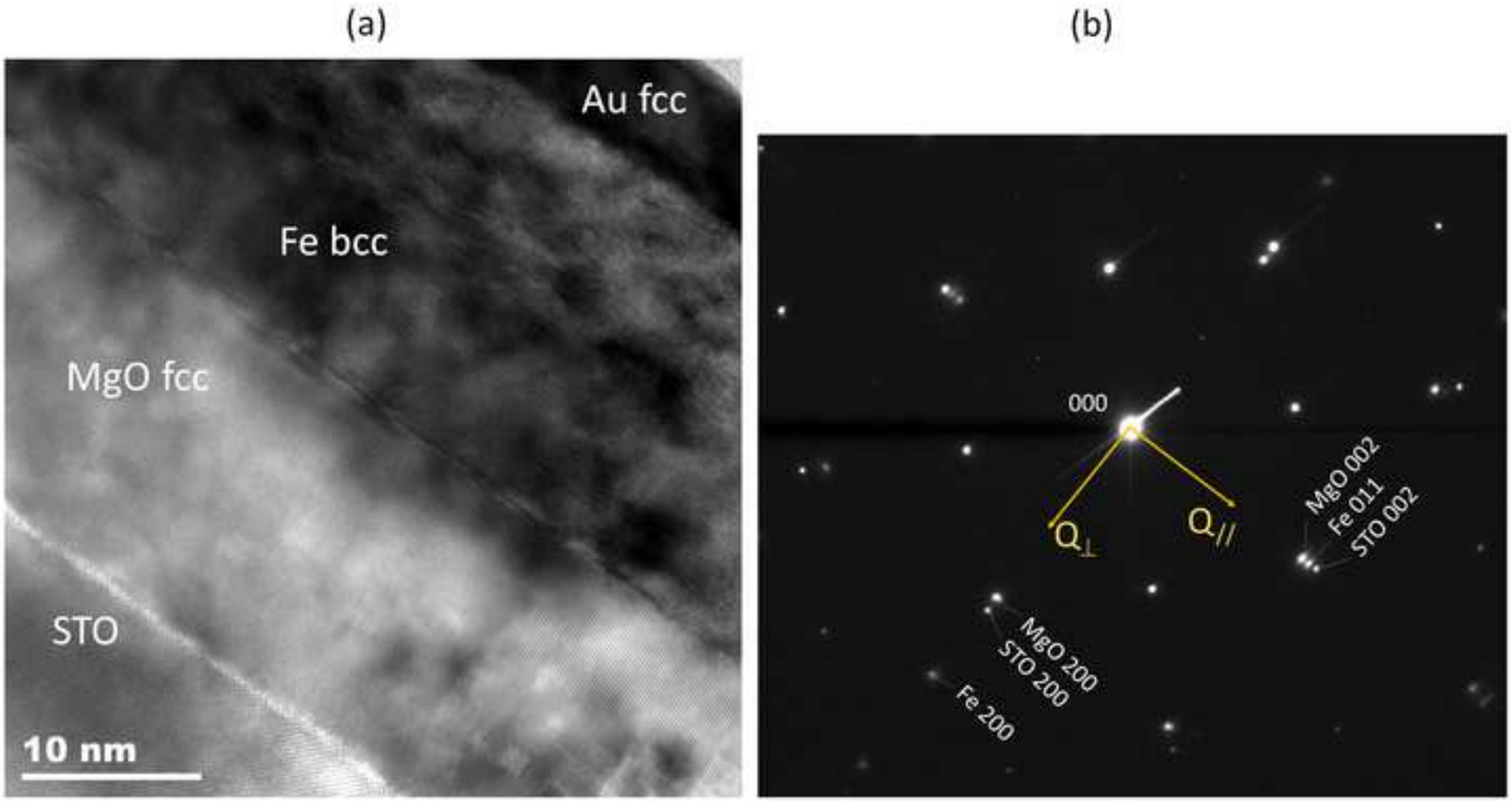

Figure 6

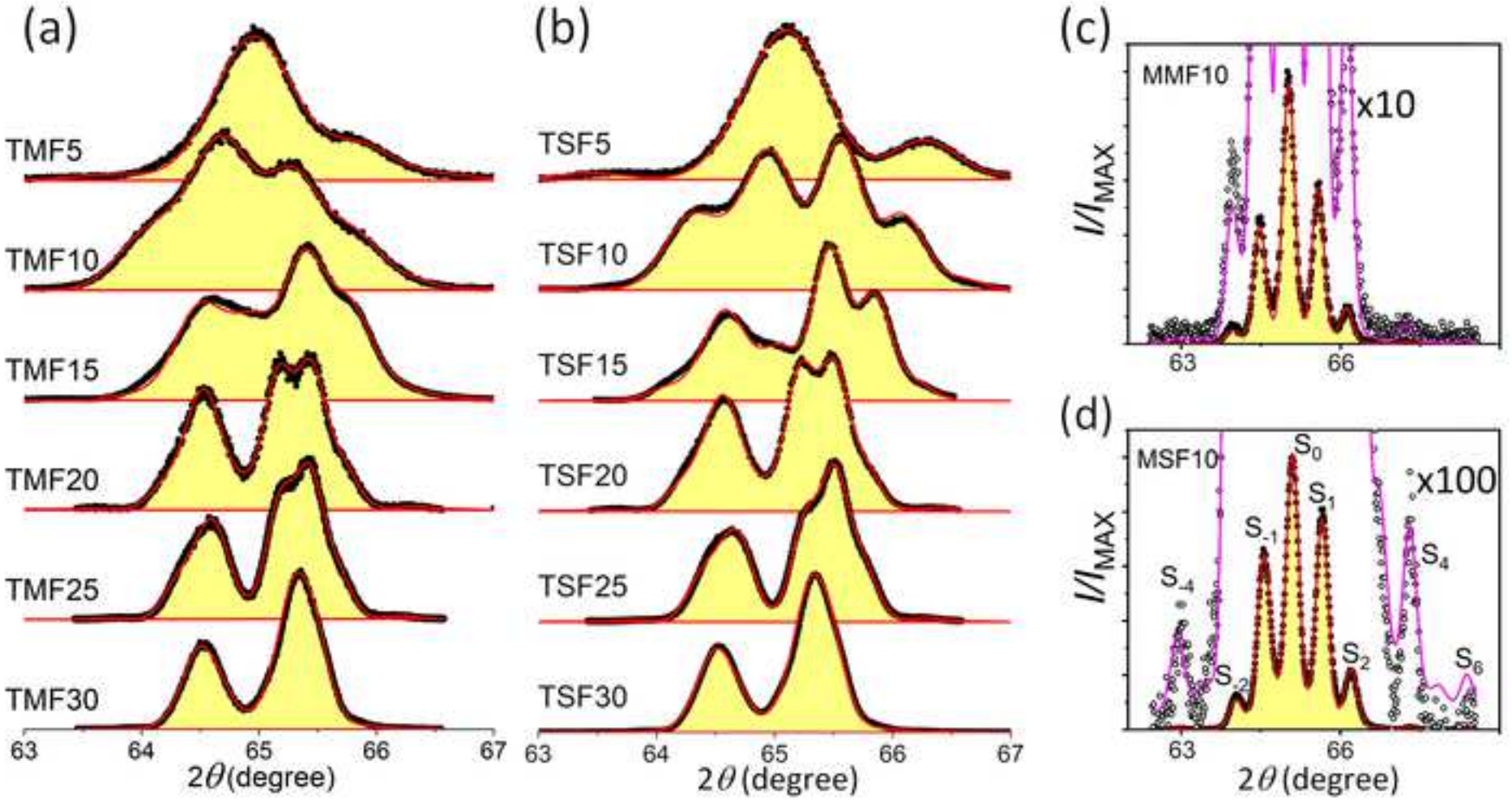

Figure 7

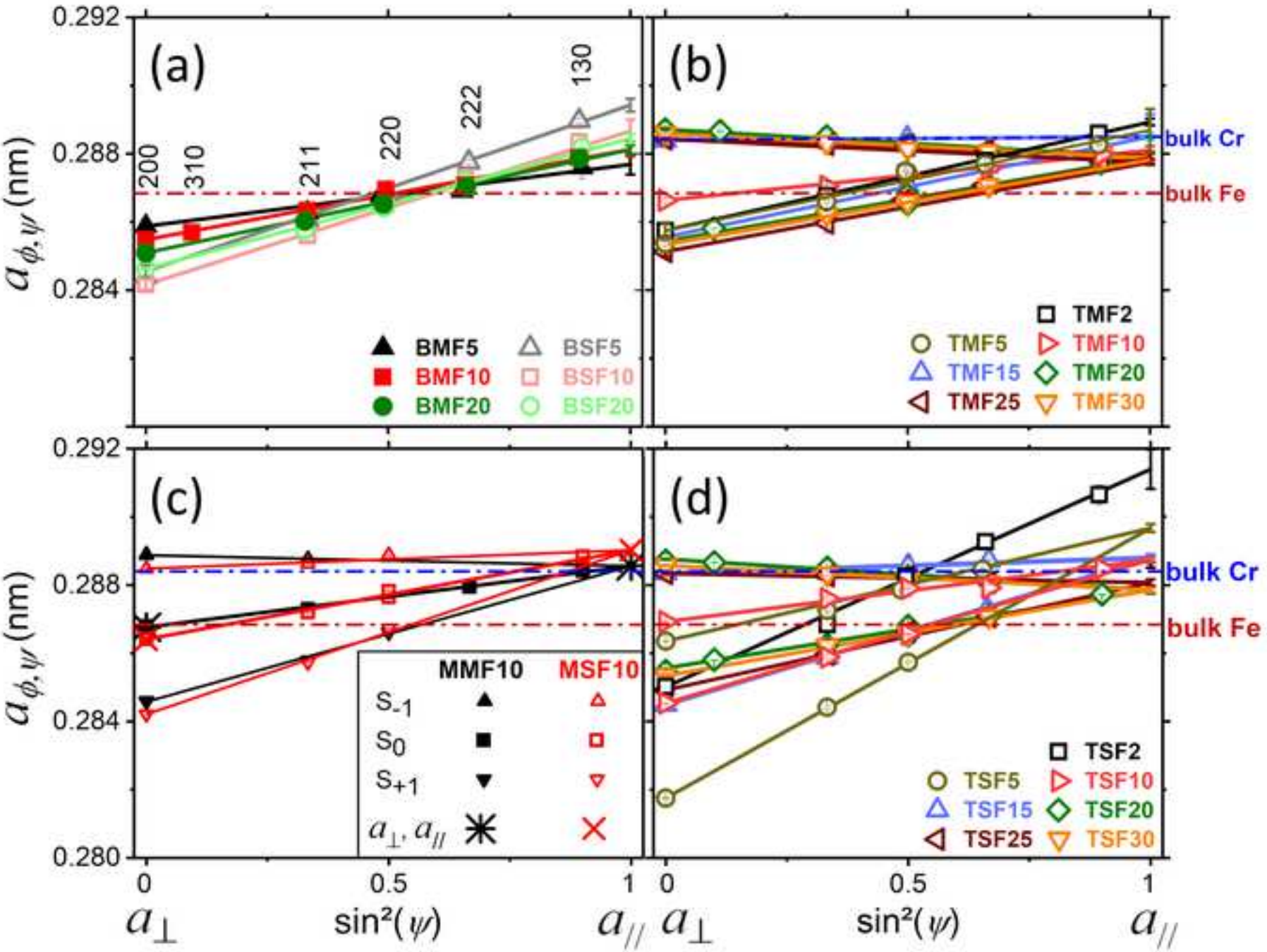

Figure 8

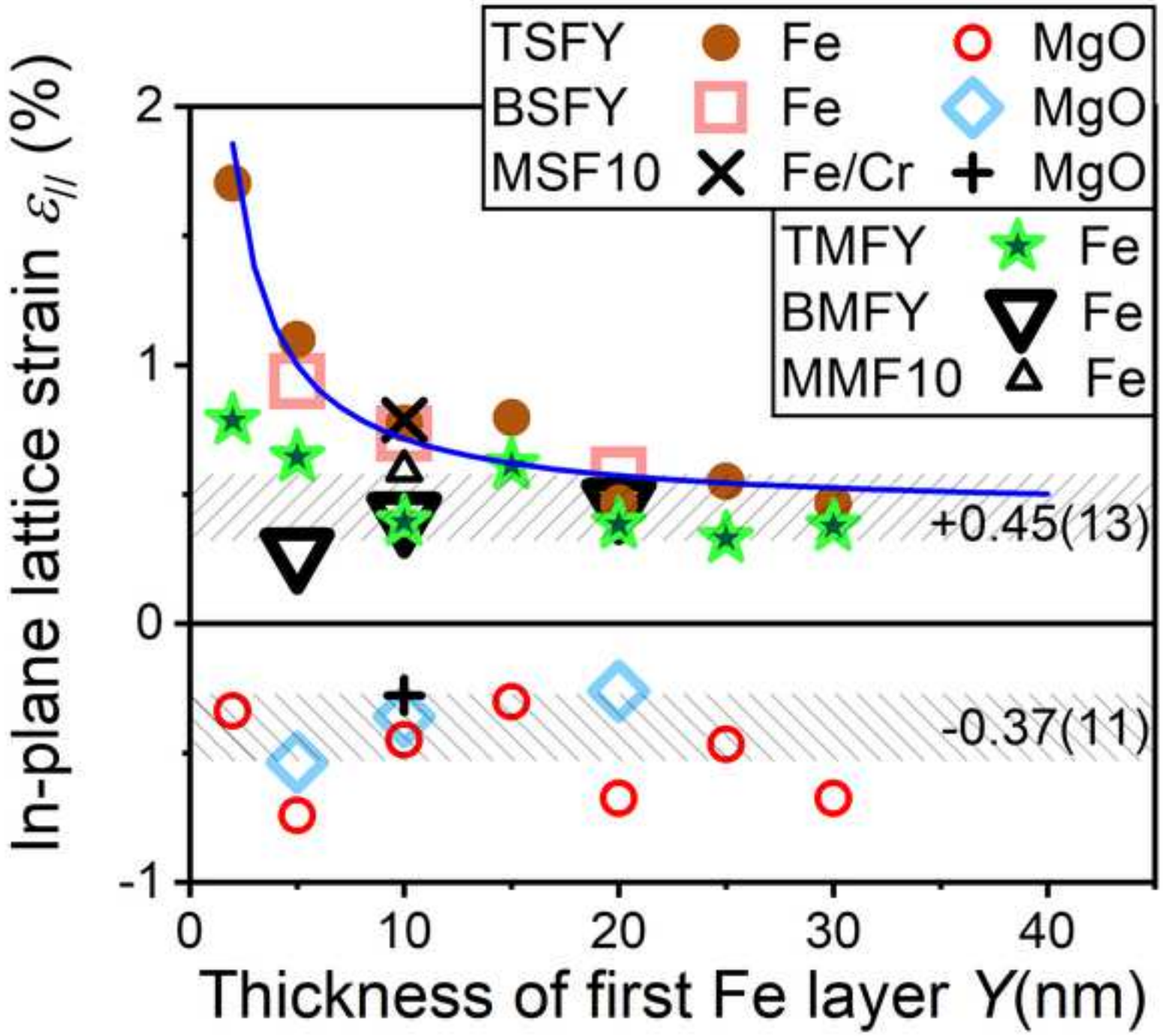

Figure 9

Click here to access/download;Figures (if any);Fig9.jpg

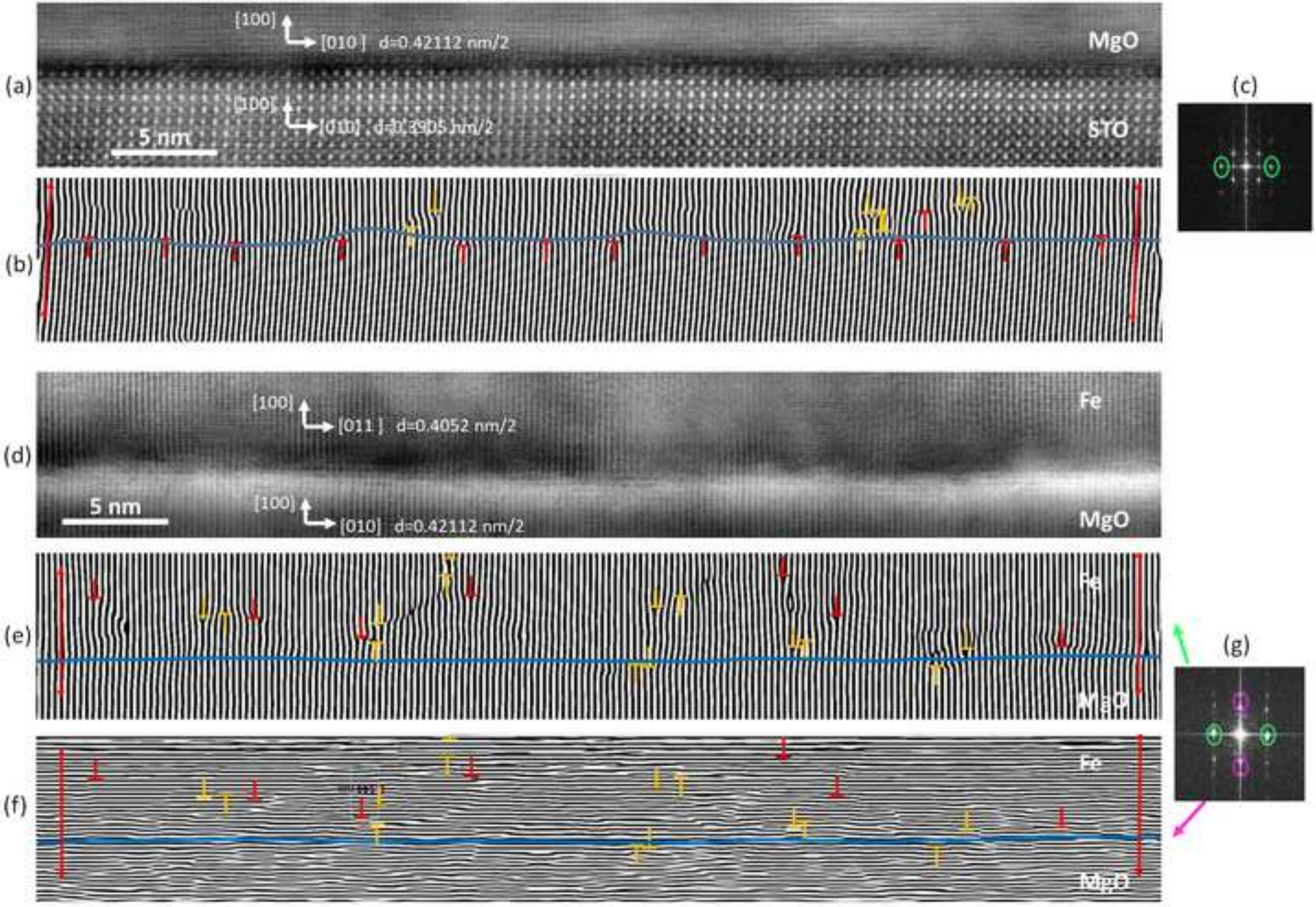

Figure 10

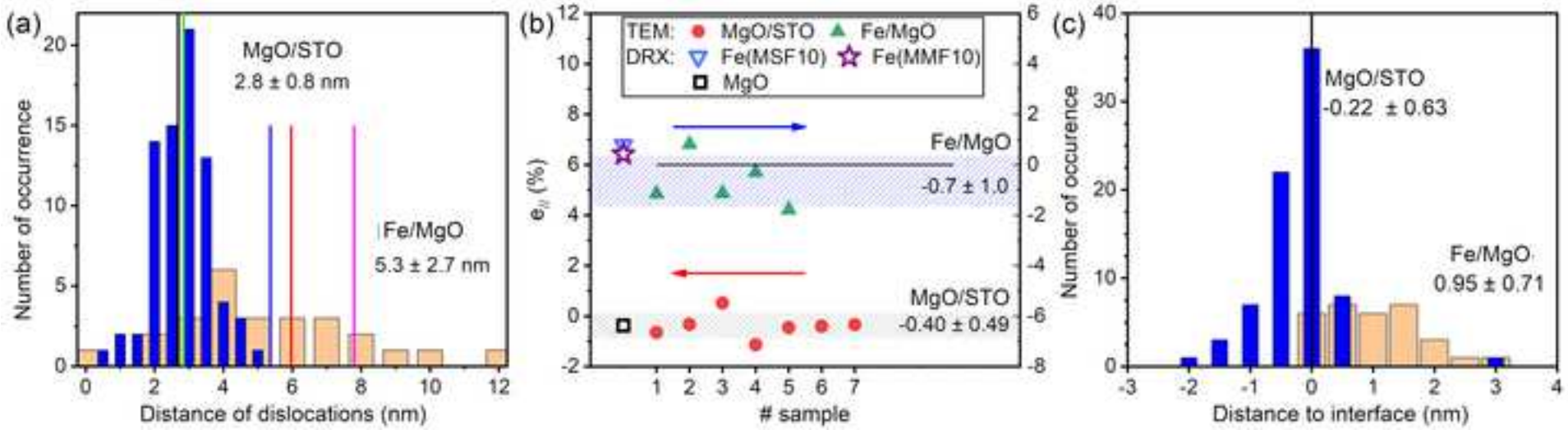

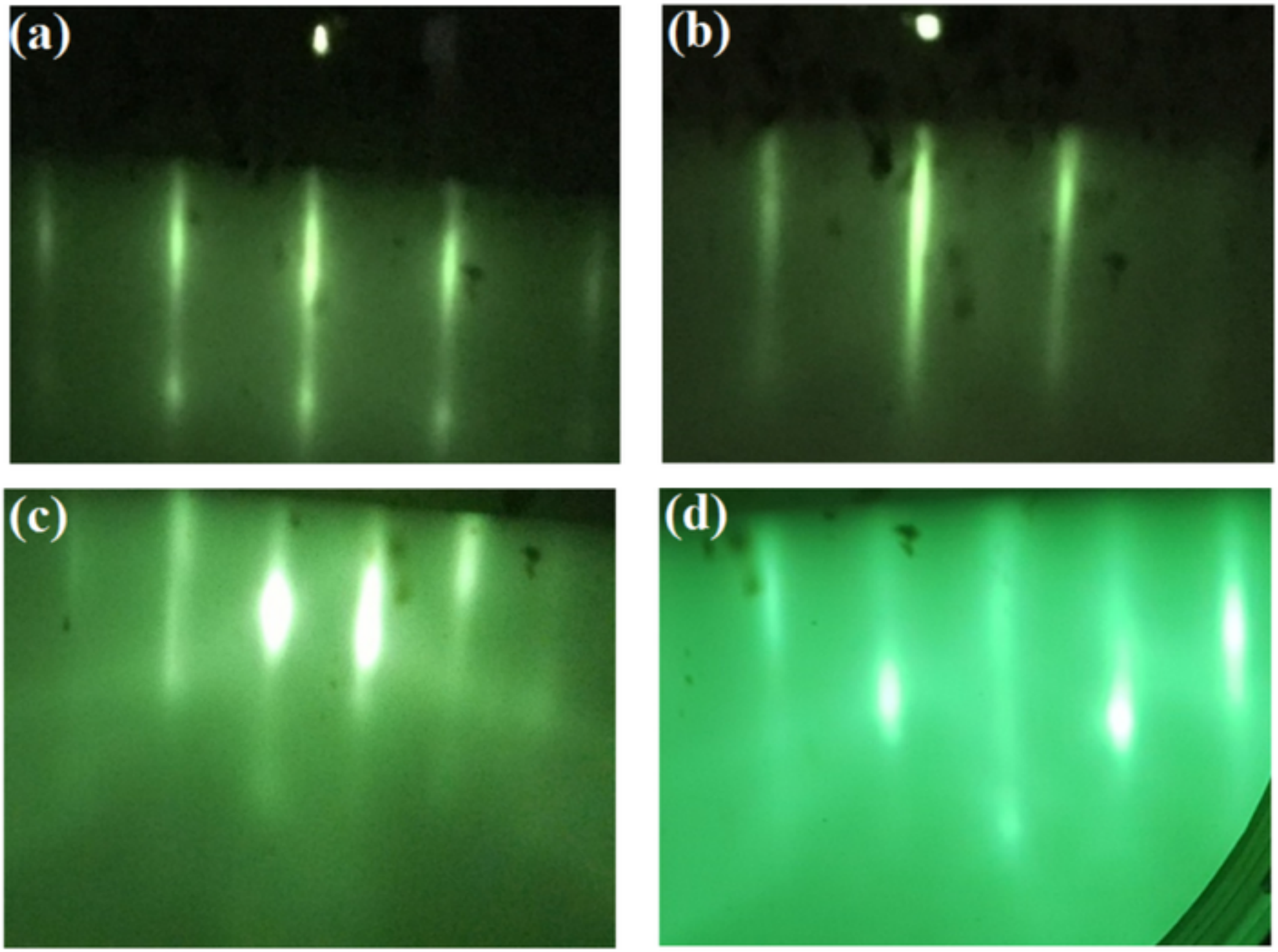

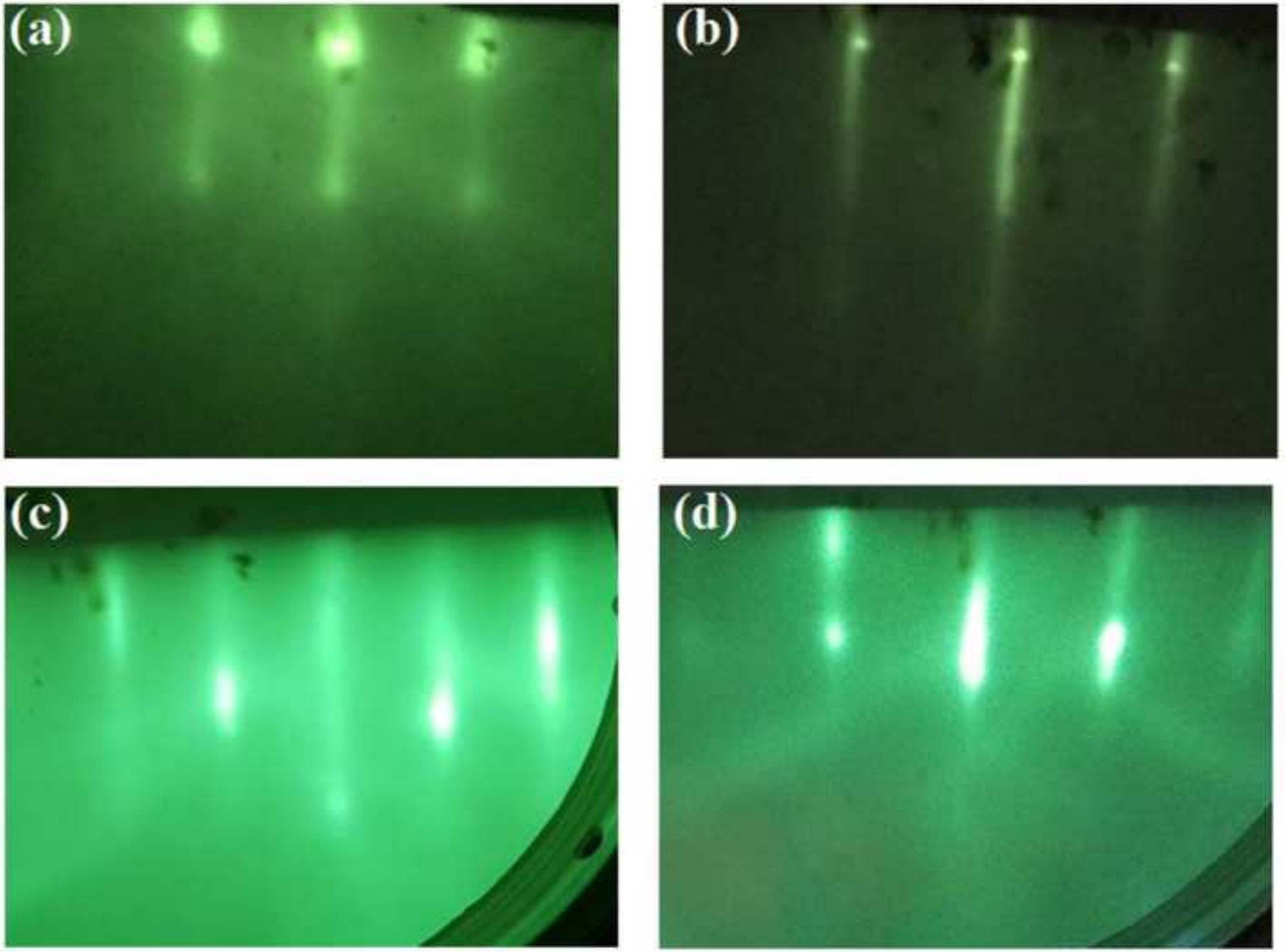

Figure A2

Click here to access/download;Figures (if any);FigA2abcd_se.jpg

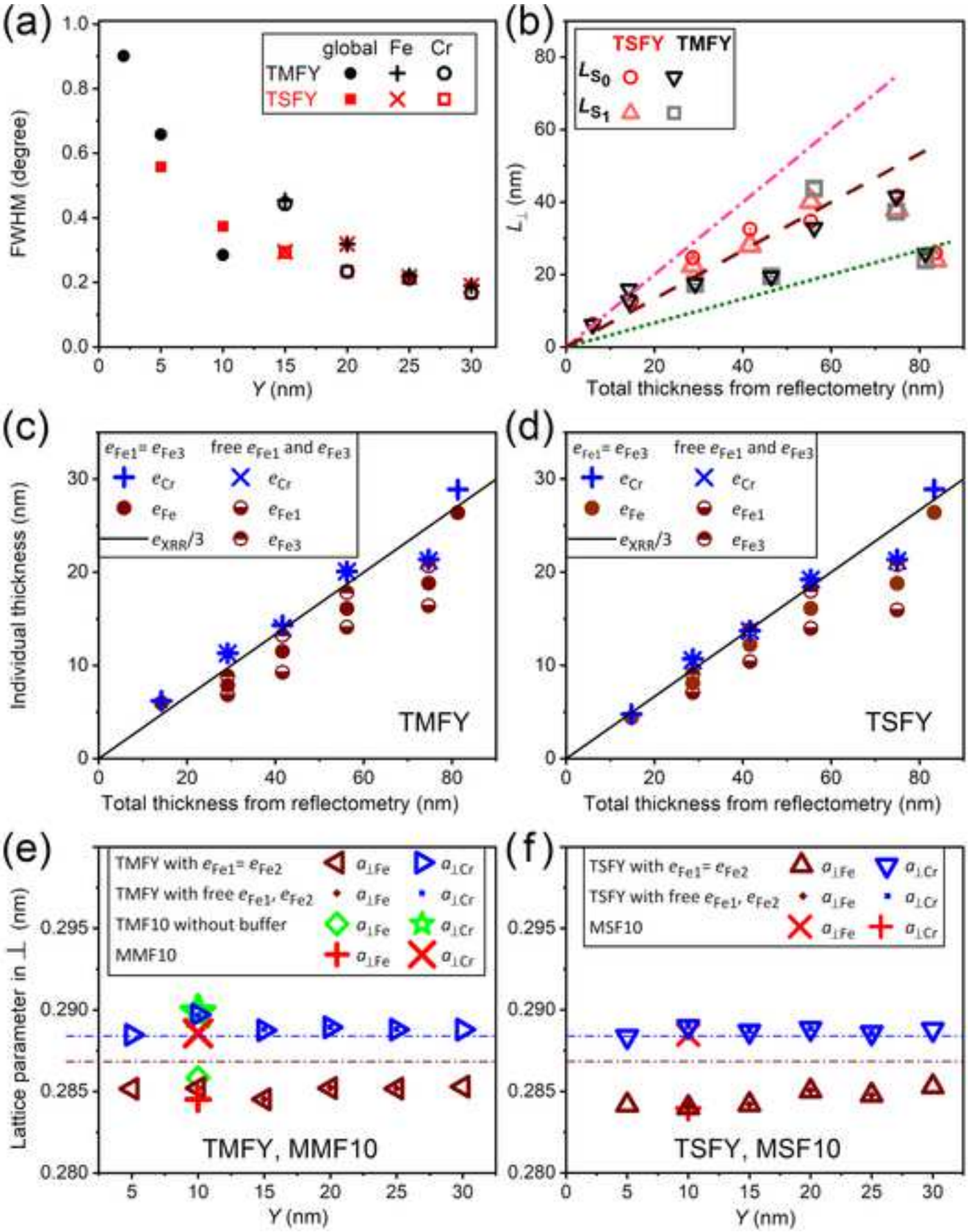

Figure A3

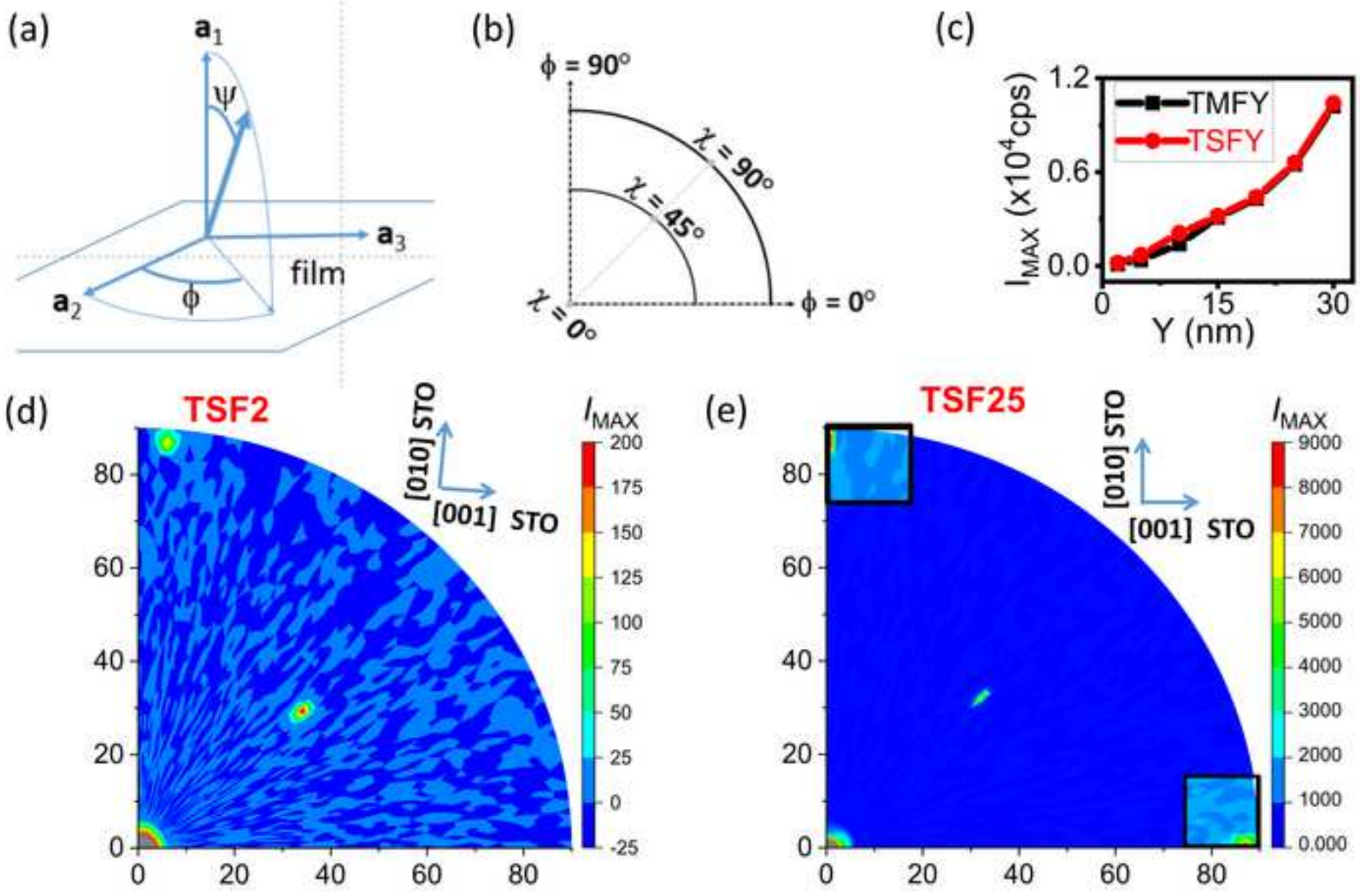

Figure A4

Click here to access/download;Figures (if any);FigA4_se.jpg

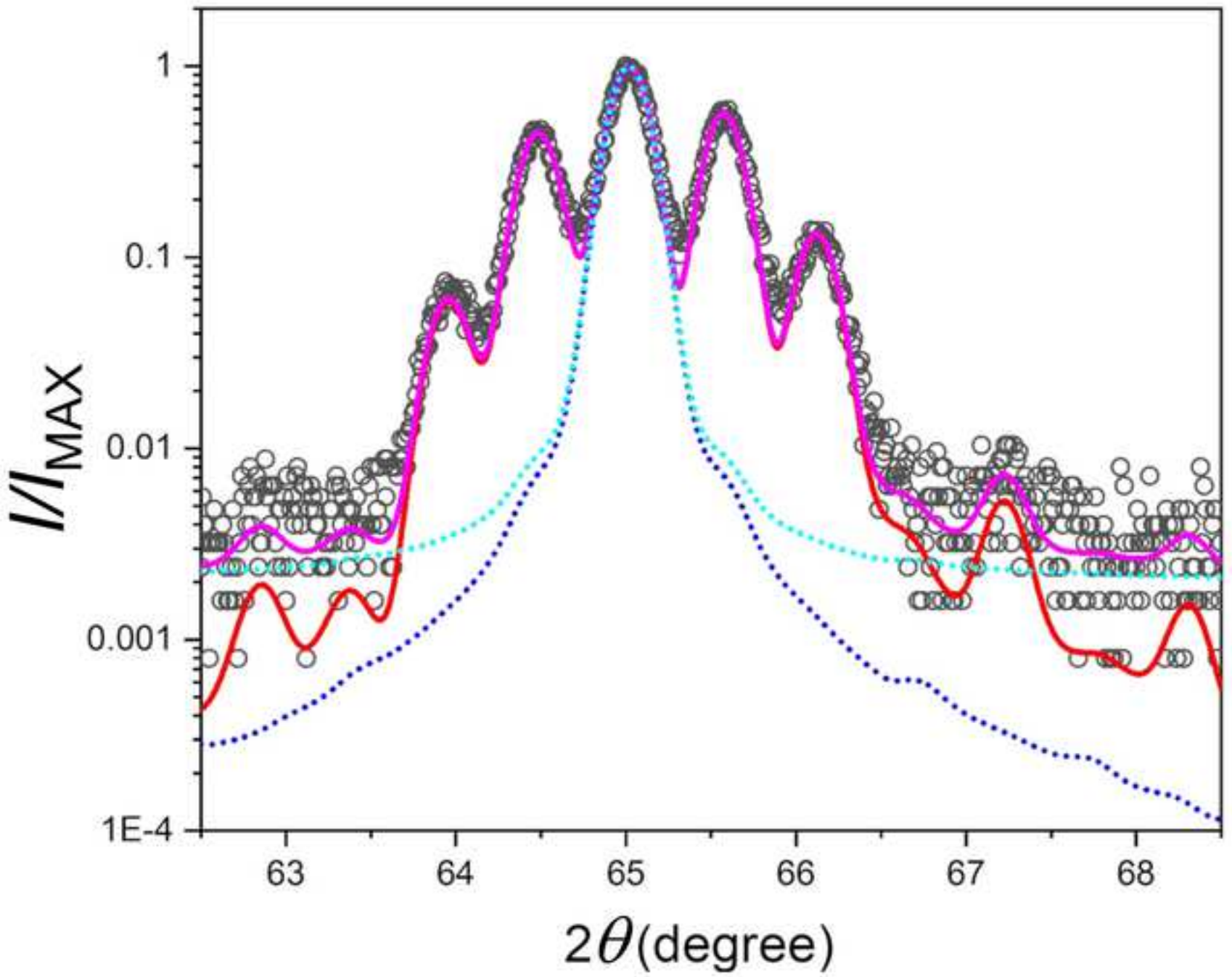

Figure A5

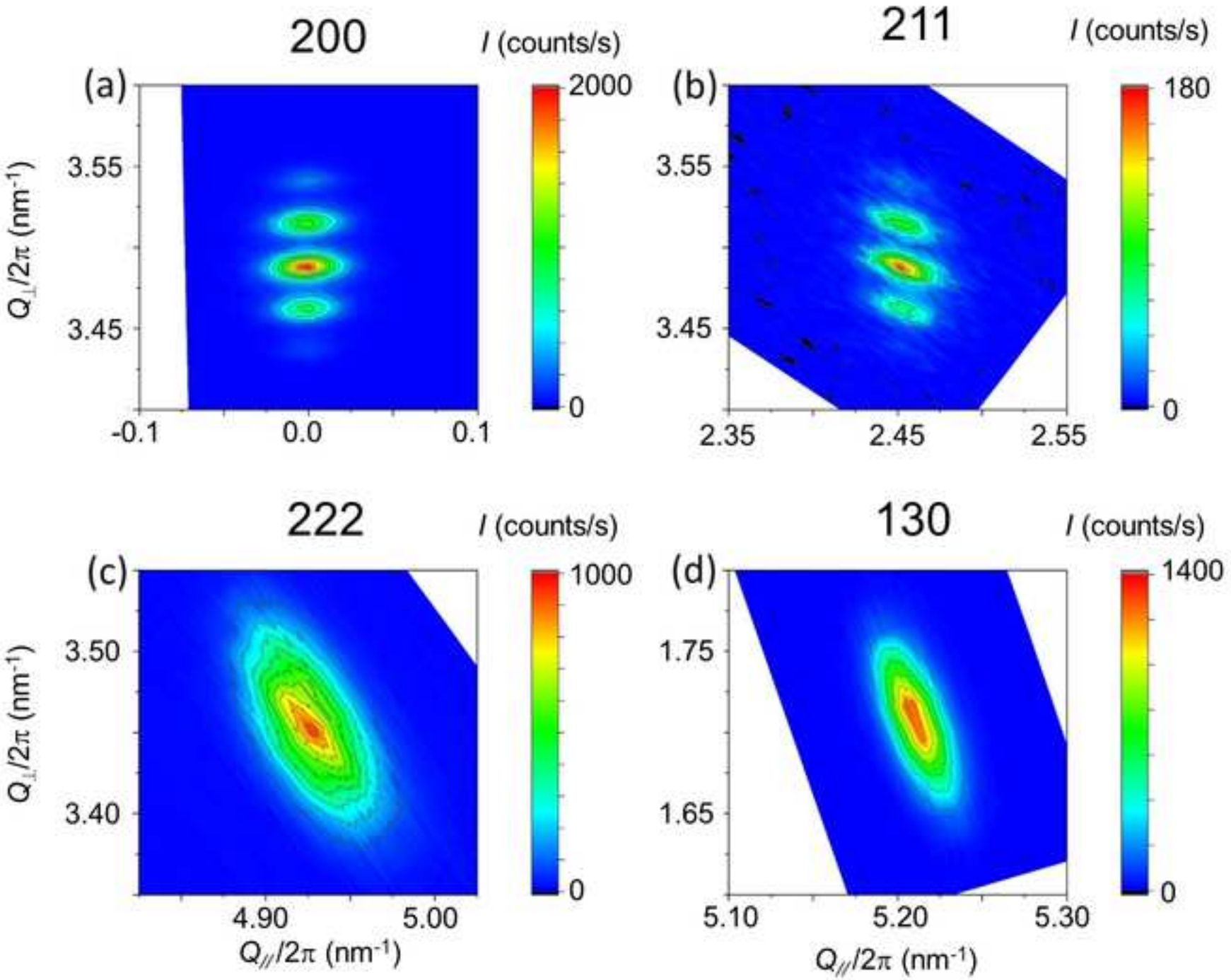

Figure A6

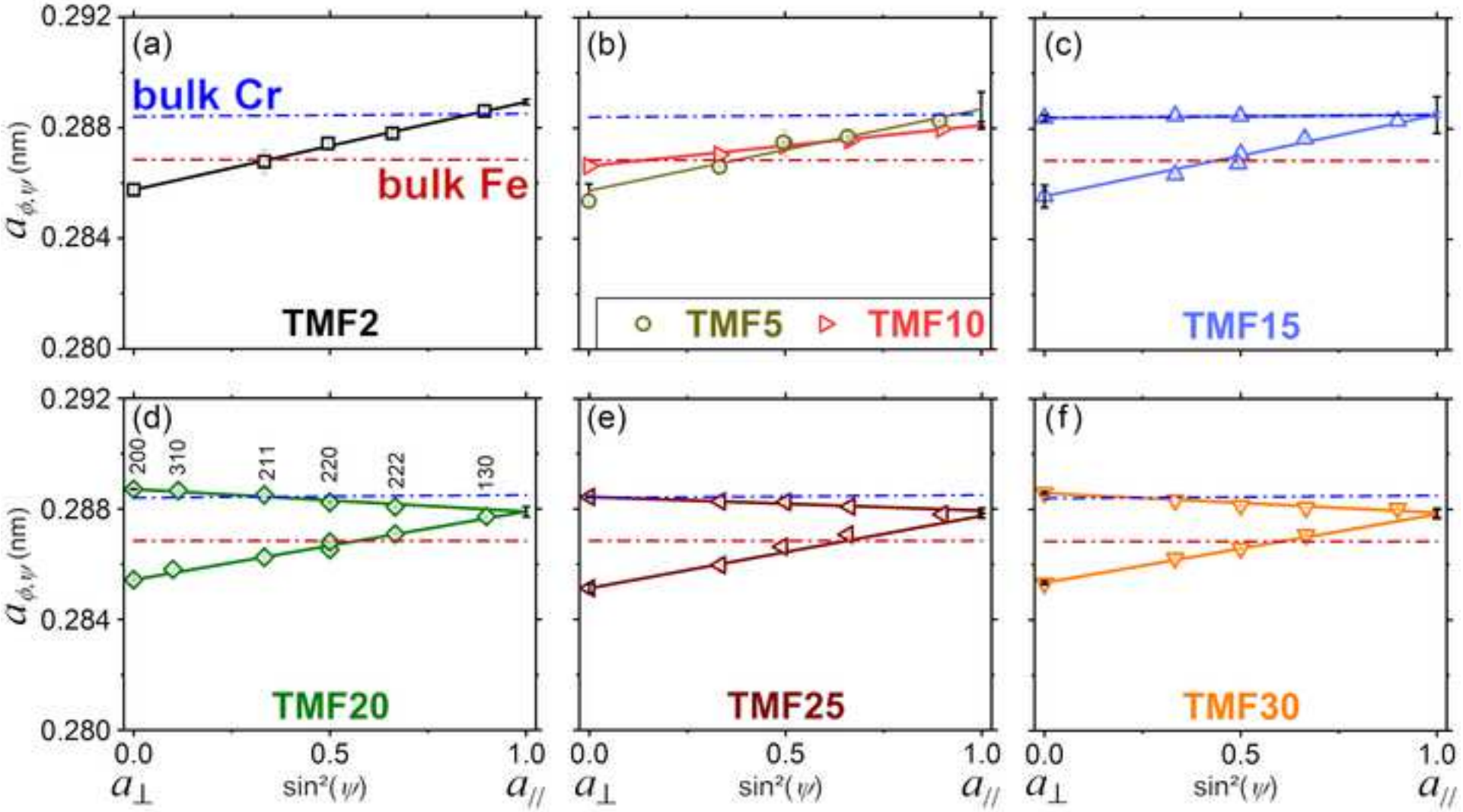

Figure A7

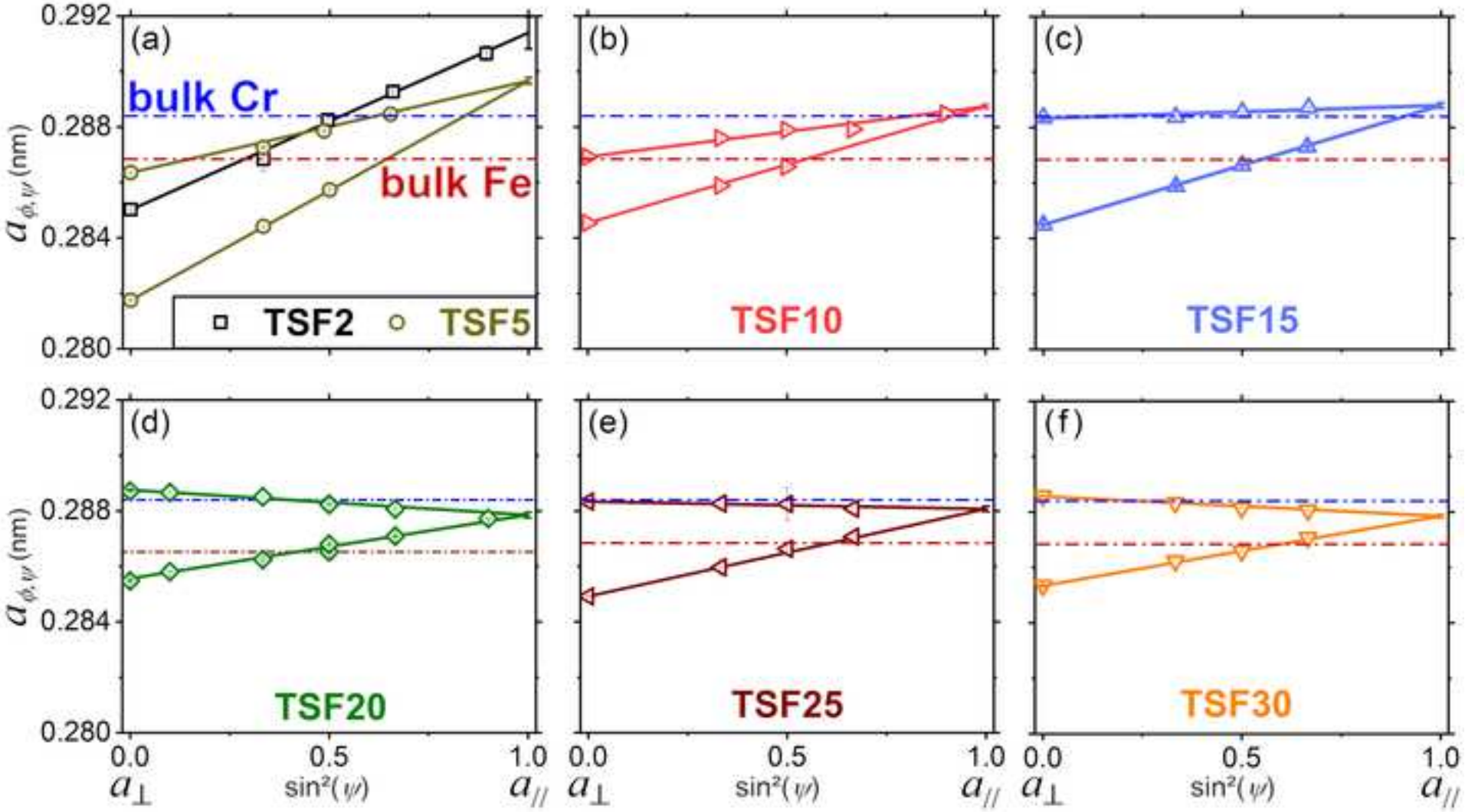

Figure A8

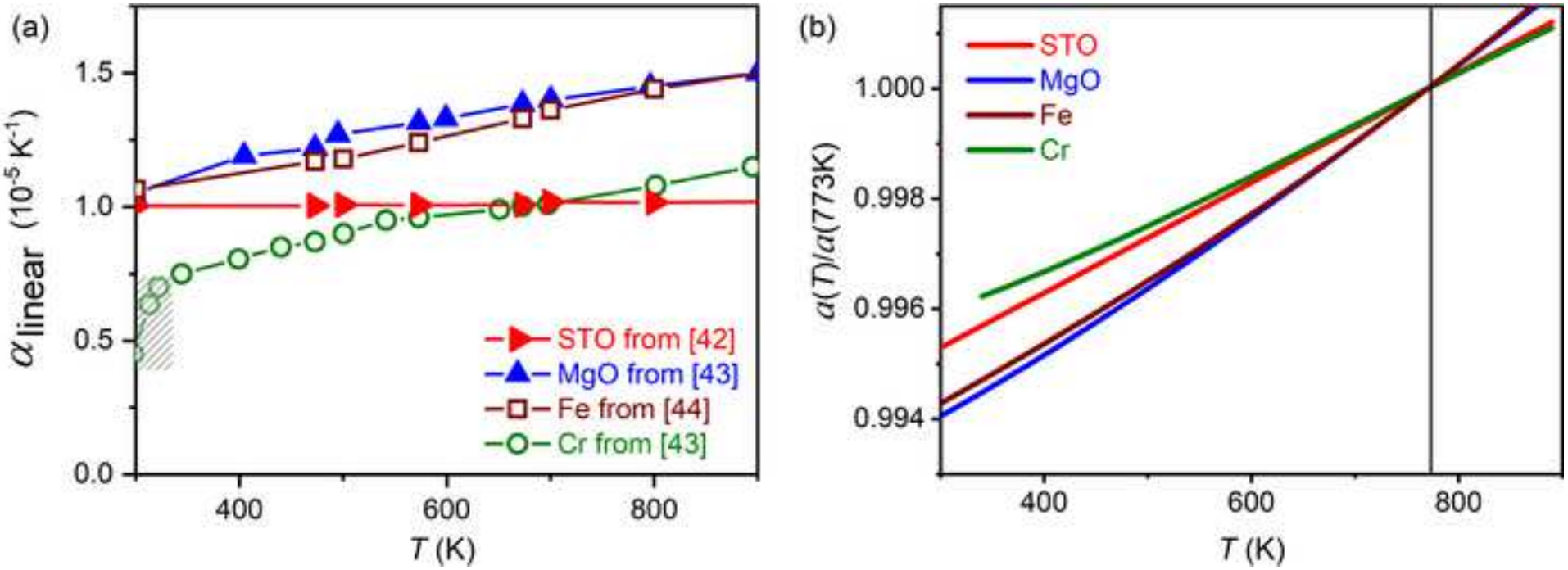

Figure A9

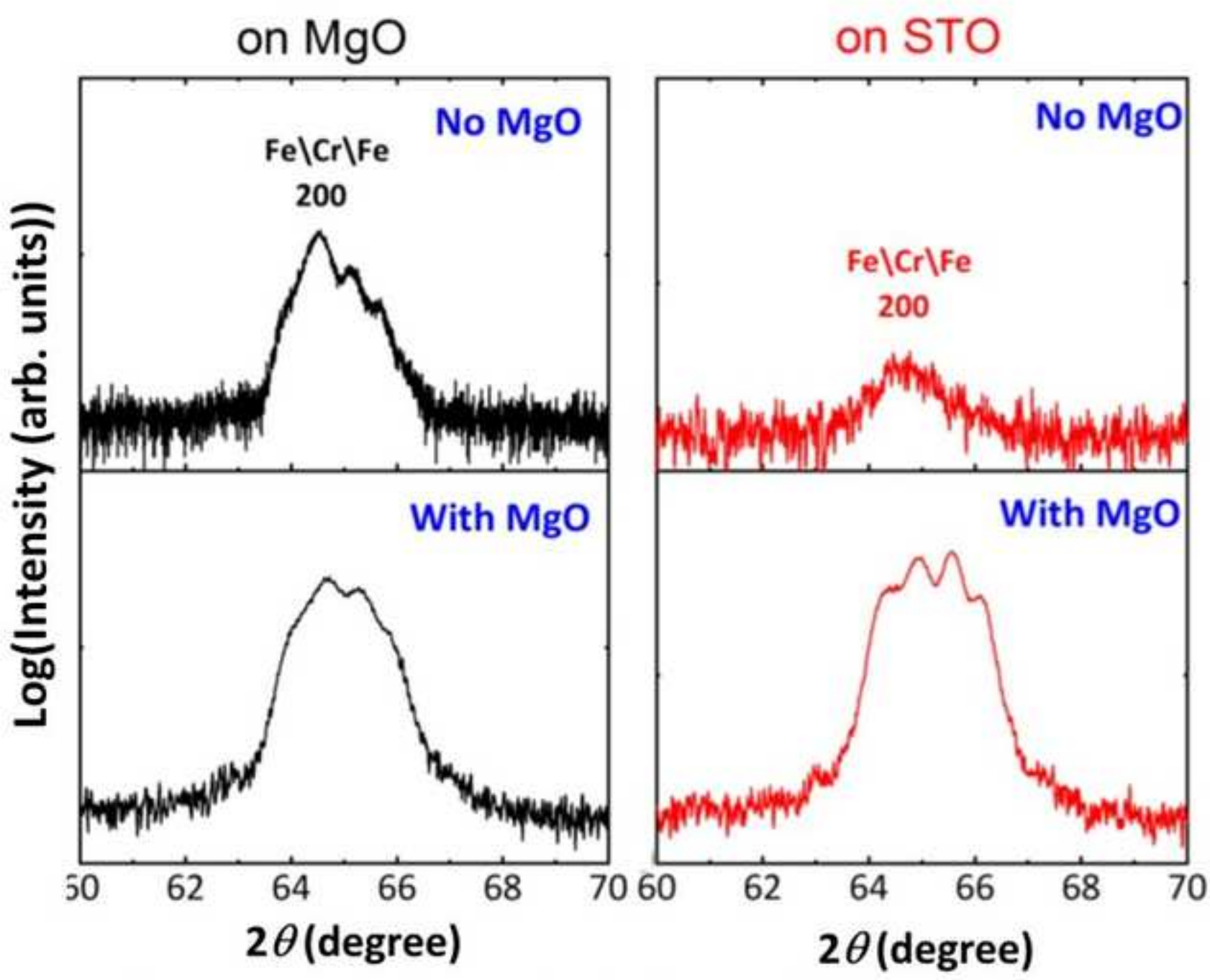

Figure A10